RIGID MODE BALLOONING INSTABILITY CALCULATION FOR THE MMX

by

B. K. Kang

Memorandum No. UCB/ERL M84/68

23 August 1984

ELECTRONICS RESEARCH LABORATORY

College of Engineering
University of California, Berkeley
94720

RIGID MODE BALLOONING INSTABILITY CALCULATION FOR THE MMX

B. K. Kang

Department of Electrical Engineering and Computer Sciences
and the Electronics Research Laboratory
University of California, Berkeley, CA 94720

Abstract

The rigid mode ballooning equation, derived by Kaiser et al., is modified to calculate the MHD growth rate in the Multiple Mirror Experiment (MMX). Numerical results are compared with the experimental data of the rigid ($m=1$) mode instability. In the model the pressure is taken to be isotropic and constant along the axis, except in the diverging field regions at the ends of the machine where the pressure falls to maintain beta constant, consistent with experimental observations. The calculated results generally predict somewhat higher critical betas for the rigid mode than those observed.

I. Introduction

In the Berkeley 10 meter Multiple Mirror Experiment (MMX) geometry, the symmetry breaking quadrupole field is weak compared to the main axisymmetric field, and the radius of curvature of the main field is large compared with characteristic radial lengths [1]. We therefore assume a paraxial approximation [2] throughout the analysis.

In the MHD approximation, the high azimuthal modes are most unstable. However, FLR corrections show that short wavelength modes are stabilized down to mode numbers so small as to violate eikonal approximation [3,4,5,6]. For a rigid perturbation, i.e., a perturbation in which the MHD displacement $\bar{\xi}$ varies only as a function of distance along the magnetic axis, there are no FLR effects since ions and electrons with their different orbits still feel the same force. This is the principal mode observed experimentally in the MMX experiment [1].

Using Newcomb's ideal MHD energy principle of the plasma in the paraxial approximation [2], we add the inertia term to the rigid mode ballooning equation [3]. A computer code, used originally to investigate high mode number ballooning instability on tandem mirrors (Kaiser's code) [7], was modified to accommodate multiple mirror configurations and rigid mode features. The finite beta equilibrium used in the calculation includes the long-thin modification of the mod-B surfaces but assumes no changes on the equilibrium ellipticity from that of the vacuum field. The pressure is taken to be isotropic, with a Gaussian radial profile, and constant along the axis except in the diverging field regions at the ends of the machine where the pressure falls to maintain beta constant, in rough agreement with experimental observations [1]. The temperature is assumed constant along the axis.

In Section II, we derive the rigid mode ballooning mode equation by using the standard definitions of the flux coordinates [2,3,8,9] to describe a quadru-

pole imposed mirror geometry, and by using Newcomb's MHD principle in the long-thin geometry. In Section III, we describe the experimental configurations and observations in the MMX [1]. In Section IV, we describe the code modification from the high mode number ballooning code to the rigid mode ballooning code, calculate averaged quantities for the rigid mode ballooning code, and compare the predicted result to the observed experimental data. In Section V, we discuss our results.

II. Theory

We use the standard definitions of flux coordinates (ψ,ϑ,l) to describe a quadrupole imposed mirror geometry. The flux coordinates are chosen such that

$$\vec{B} = \nabla\psi \times \nabla\vartheta \tag{1}$$

where, ψ is a coordinate describing the axial magnetic flux, ϑ is an angle-like coordinate with period 2π on each ψ surface, and l is distance measured along a field line on which ψ and ϑ are constant.

For long-thin geometry, the field-line is nearly parallel to the axis of the machine and the transformation to cartesian coordinates (x,y,z) is based on the familiar paraxial approximation [2,3,7,9]

$$\begin{aligned} x &= \sqrt{2\psi}\,\sigma(z)\cos\vartheta, \\ y &= \sqrt{2\psi}\,\tau(z)\sin\vartheta, \\ z &= l, \end{aligned} \tag{2}$$

where σ and τ satisfy

$$\sigma\tau = \frac{\partial(x,y)}{\partial(\psi,\vartheta)} \equiv \frac{1}{B}. \tag{3}$$

Note that the functional rotation between (x,y) and (ψ,ϑ) can also be written as

$$\frac{\partial\psi}{\partial x} = By_{\vartheta}, \quad \frac{\partial\psi}{\partial y} = Bx_{\vartheta},$$
$$\frac{\partial\vartheta}{\partial x} = -By_{\psi}, \quad \frac{\partial\vartheta}{\partial y} = Bx_{\psi}, \tag{4}$$

where, the subscripts denote partial derivatives with respect to the indicated variables. By choosing contravariant basis vectors as $(\nabla\psi, \nabla\vartheta, \hat{z})$, i.e.,

$$\nabla\psi = \left[\frac{\partial\psi}{\partial x}, \frac{\partial\psi}{\partial y}\right] = B(y_{\vartheta}, -x_{\vartheta})$$
$$= \frac{\sqrt{2\psi}}{\sigma\tau}(\tau\cos\vartheta, \sigma\sin\vartheta), \tag{5}$$

$$\nabla\vartheta = \left[\frac{\partial\vartheta}{\partial x}, \frac{\partial\vartheta}{\partial y}\right] = B(-y_{\psi}, x_{\psi})$$
$$= \frac{1}{\sqrt{2\psi}\sigma\tau}(-\tau\sin\vartheta, \sigma\cos\vartheta), \tag{6}$$

the covariant basis vectors become

$$\bar{u} = -B^{-2}\bar{B}\times\nabla\vartheta = (x_{\psi}, y_{\psi})$$
$$= \frac{1}{\sqrt{2\psi}}(\sigma\cos\vartheta, 2\sin\vartheta), \tag{7}$$

$$\bar{v} = B^{-2}\bar{B}\times\nabla\psi = (x_{\vartheta}, y_{\vartheta})$$
$$= \sqrt{2\psi}(-\sigma\sin\vartheta, \tau\cos\vartheta). \tag{8}$$

The covariant metric tensor is given as

$$\tilde{g} = \begin{bmatrix} \bar{u}\cdot\bar{u} & \bar{u}\cdot\bar{v} & 0 \\ \bar{u}\cdot\bar{v} & \bar{v}\cdot\bar{v} & 0 \\ 0 & 0 & 1 \end{bmatrix} \equiv \begin{bmatrix} E & F & 0 \\ F & G & 0 \\ 0 & 0 & 1 \end{bmatrix} \tag{9}$$

$$\|g\| = \frac{1}{B^2}$$

where

$$E = \bar{u}\cdot\bar{u} = B^{-2}\nabla\vartheta\cdot\nabla\vartheta,$$

$$F = \bar{u}\cdot\bar{v} = -B^{-2}\nabla\psi\cdot\nabla\vartheta, \tag{10}$$

$$G = \bar{v}\cdot\bar{v} = B^{-2}\nabla\psi\cdot\nabla\psi.$$

The covariant components of the curvature vector are given by

$$\bar{\kappa} = (x_{zz}, y_{zz}) = \kappa_\psi\nabla\psi + \kappa_\vartheta\nabla\vartheta \tag{11}$$

where

$$\kappa_\psi = \bar{\kappa}\cdot\bar{u} = x_\psi x_{zz} + y_\psi y_{zz},$$

$$\kappa_\vartheta = \bar{\kappa}\cdot\bar{v} = x_\vartheta x_{zz} + y_\vartheta y_{zz}, \tag{12}$$

The quantities κ_ψ and κ_ϑ are the normal and the geodesic curvatures, respectively.

For a finite beta plasma, we assume no change in equilibrium ellipticity from that of the vacuum geometry described by (2). W. A. Newcomb [2]. derived the ideal MHD energy principle of the plasma in the long-thin approximation

$$\delta H = \delta T + \delta W = 0, \tag{13}$$

$$\delta T = \frac{1}{2}\int \rho(EX_t^2 + 2FX_t Y_t + GY_t^2)\frac{d\psi d\vartheta dz}{B}, \tag{14}$$

$$\delta W = \frac{1}{2}\int [Q(EX_z^2 + 2FX_z Y_z + GY_z^2)$$

$$-2\frac{\partial P}{\partial\psi}X(\kappa_\psi X + \kappa_\vartheta Y) + (X_z Y - XY_z)]\ \frac{d\psi d\vartheta dz}{B}, \tag{15}$$

where H is the energy integral, T is the kinetic energy, and W is the effective potential energy of the linearized equation of motion, respectively. Here $P \equiv \frac{1}{2}(P_\perp + P_\parallel)$, $Q \equiv B^2 + P_\perp - P_\parallel, i$ is the parallel current per unit flux, and ρ is the mass density inside the plasma. Also, X and Y are the contravariant components of the small displacement $\bar{\xi}$ defined as

$$X = \nabla\psi\cdot\bar{\xi},$$
$$Y = \nabla\vartheta\cdot\bar{\xi}. \tag{16}$$

Note that the parallel curent i is zero for a low-beta plasma in the geometry (2)

$$\begin{aligned} i &= \hat{b}\cdot\nabla\times\hat{b} = -\frac{\partial x_z}{\partial y} + \frac{\partial y_z}{\partial x} \\ &= B(x_{z\psi}x_\vartheta + y_{z\psi}y_\vartheta - x_{z\vartheta}x_\psi - y_{z\vartheta}y_\psi) \\ &= 0. \end{aligned} \tag{17}$$

For a rigid perturbation

$$\bar{\xi} = (\sigma u, \tau v)$$

with $u(z)$ and $v(z)$ arbitrary, X and Y become

$$X = \sqrt{2\psi}(u\cos\vartheta + v\sin\vartheta),$$
$$Y = \frac{1}{\sqrt{2\psi}}(-u\sin\vartheta + v\cos\vartheta). \tag{18}$$

By putting (10), (12) and (18) into (14) and (15), we have δT and δW inside the plasma as

$$\delta T = \pi\psi_B\int\frac{dz}{B}\langle\rho\rangle(\sigma^2 u_t^2 + \tau^2 v_t^2), \tag{19}$$

$$\delta W = \pi\psi_B\int\frac{dz}{B}\{\langle Q\rangle(\sigma^2 u_z^2 + \tau^2 v_z^2) + \langle P\rangle(u^2\sigma\sigma'' + v^2\tau\tau'')\} \tag{20}$$

where

$$\langle Q\rangle \equiv \int_0^{\psi_B}\frac{d\psi}{\psi_B}Q,$$
$$\langle P\rangle \equiv \int_0^{\psi_B}\frac{d\psi}{\psi_B}P,$$
$$\langle\rho\rangle \equiv \int_0^{\psi_B}\frac{d\psi}{\psi_B}\rho.$$

The 1st and 2nd terms of (20) are the line-bending and driving energy, respec-

tively. For a rigid perturbation, the vacuum contribution to the line-bending energy is important. Kaiser et al. [3] derived the vacuum contribution to the line-bending energy, under the assumption that a perfectly conducting wall exists at $\psi = \psi_W$, as

$$\delta W_v = \pi\psi_B \int dz\, \eta (u_z^2 + v_z^2) \tag{21}$$

where

$$\eta = \frac{2(\psi_W/\psi_B)+[4(\psi_W/\psi_B)^2+B^2(\sigma^2-\tau^2)^2]^{1/2} + B(\sigma+\tau)^2}{2(\psi_W/\psi_B) + [4(\psi_W/\psi_B)^2 + B^2(\sigma^2-\tau^2)^2]^{1/2}-B(\sigma+\tau)^2} .$$

Now, the Lagrangian $L = \delta T - \delta W$ is

$$L = \omega^2\pi\psi_B \int \frac{dz}{B}(\sigma^2 u^2+\tau^2 v^2)\langle\rho\rangle$$

$$-\pi\psi_B \int dz \left[\left[\frac{\langle Q\rangle}{B}\sigma^2+\eta\right]u_z^2 + \left[\frac{\langle Q\rangle}{B}\tau^2 + \eta\right]v_z^2\right.$$

$$\left. +2\frac{\langle P\rangle}{B}(\sigma\sigma'' u^2+\tau\tau'' v^2)\right]$$

and the Euler-Lagrange equation gives the rigid mode ballooning equation as

$$\frac{d}{dz}\left[\left[\frac{\langle Q\rangle}{B}\sigma^2+\eta\right]\frac{du}{dz}\right] + \omega^2\frac{\langle\rho\rangle}{B}\sigma^2 u - 2\frac{\langle P\rangle}{B}\sigma\sigma'' u = 0 \tag{22}$$

III. Experiment

Ballooning instabilities in the MMX have been experimentally studied by Price et al. [1]. The standard stabilized multiple-mirror magnetic field consists of a one meter guide field section and a series of mirror cells, as indicated in Fig. 1. The axial field consists of a uniform solenoid and nine sharp mirrors whose 75 cm spacing determines the cell length. Two sets of currents, a weak and a strong quadrupole, are also present on each cell, and reverse polarities between cells. The weak quadrupole bars extend over the midplane regions and

provide weakly good curvature through most of the cell length. The shorter strong quadrupoles are located near each mirror throat and provide strong good curvature necessary to counter the effect of the mirror coils. The quadrupole currents can be optimized to give the best average minimum-B operation [11].

Four field configurations, modified from the standard field, with varying curvature derive and connection lengths, are employed to experimentally investigate critical betas (β_c) for ballooning. In configuration (i) the linked quadrupole current of the multiple mirror field is varied to weaken and reverse the good curvature in the midplane region of each cell. This configuration is the standard MMX configuration if the quadrupole currents are optimized.

In configuration (ii) the vacuum curvature is modified to create a weakly unstable region in two adjacent cells by removing the quadrupole and mirror current between midplanes M_{12} and M_{34}, leaving only the solenoid field, while maintaining favorable curvature in the cells bounding this region. Weak bad curvature occurs in the transitions between the solenoid and the bounding good curvature regions, similar to a tandem mirror configuration. A sketch of the flux surfaces is given in Fig. 2. The mode amplitude is large at M_{23}, the midplane in the center of the bad curvature region and much smaller at M_{45}, a midplane with good curvature. The observed critical beta for configuration (ii), with mirror ratio 3 and with reduced quadrupoles (80% of the optimized values), is 15%. The plasma motion has both radial and azimuthal components indicating that the corresponding real and imaginary parts of the frequency are comparable. This implies non-ideal MHD effects are comparable to ideal MHD effects.

In configuration (iii) the weak quadrupole fields are pulsed off between midplanes M_{12} and M_{34}. The drive is larger because of the two unstabilized magnetic mirrors within the central region of configuration (iii). A sketch of flux surfaces is given in Fig. 3. Observed critical betas for this configuration are 10%

for mirror ratio 3 with reduced quadrupole current (80%), and 5% for mirror ratio 4 with full quadrupole current. Observed plasma motion is similar to that of configuration (ii), except that the unstable motion is principally radial, indicating that the imaginary part of the frequency dominates the real part.

In configuration (iv) the weak quadrupole fields are pulsed off between mirror throats T_1 and T_3. Unlike case (ii) and (iii), the amount of unfavorable curvature is strongly dependent on the azimuthal direction, with the strongly unstable direction being vertical. A sketch of flux surfaces is shown in Fig. 4. The observed critical beta is 10% for mirror ratio 4 and full quadrupole current. The observed plasma motion is in the unstable direction.

IV. Computation

We modify the existing high-mode-number ballooning code (Kaiser's code) to a rigid mode ballooning code. Kaiser's code [7] solves the eigenvalue equation in the (ψ,ϑ,z) coordinate system which has the form

$$\frac{\partial}{\partial z}\left[\frac{|\nabla S|^2}{B}\frac{Q}{B^2}\frac{\partial V}{\partial z}\right]+\left[\frac{\rho\omega^2}{B^2}\frac{|\nabla S|^2}{B} + \frac{\partial(P_\perp+P_\parallel)}{\partial\psi}\frac{S_\vartheta}{B}(S_\vartheta\kappa_\psi-S_\psi\kappa_\vartheta)\right]V=0 \tag{23}$$

where $\nabla S = S_\psi\nabla\psi + S_\vartheta\nabla\vartheta$ is the wave vector, and V is the eigenfunction which is related to the perturbed electrostatic potential φ by $\nabla_\perp\varphi = B\nabla_\perp\left[\frac{V}{B}\right]$. The eigenfrequency ω is obtained by multiplying (23) by V and integrating along a field line

$$\omega^2 = \frac{\int_{-l}^{l}\frac{dz}{B}\left[|\nabla S|^2\frac{Q}{B^2}\left[\frac{dV}{dz}\right]^2 - \frac{\partial(P_\perp+P_\parallel)}{\partial\psi}S_\vartheta(S_\vartheta\kappa_\psi-S_\psi\kappa_\vartheta)V^2\right]}{\int_{-l}^{l}\frac{dz}{B}\frac{\rho}{B^2}|\nabla S|^2V^2} \tag{24}$$

Comparing (22) with (23), we obtain a rigid mode ballooning code by replacing

$$V \to u, \frac{|\nabla S|^2}{B}\ \frac{Q}{B^2} \to \frac{\langle Q \rangle}{B}\sigma^2 + \eta \equiv \mathrm{L}, \frac{\rho}{B^3}|\nabla S|^2 \to \frac{\langle \rho \rangle}{B}\sigma^2 \equiv I, \qquad \text{and}$$

$$\frac{\partial(P_\perp + P_\parallel)}{\partial \psi}\ \frac{S_\vartheta}{B}(S_\vartheta K_\psi - S_\psi K_\vartheta) \to -2\frac{\langle P \rangle}{B}\sigma\sigma'' \equiv D,$$

$$\frac{d}{dz}\left[\mathrm{L}\frac{du}{dz}\right] + (D + \omega^2 I)u = 0 \tag{25}$$

The averaged quantities $\langle \rho \rangle$, $\langle P \rangle$, and $\langle Q \rangle$ are calculated under the assumptions that the pressure profile is isotropic and Gaussian, and that the density depends only on ψ

$$\begin{aligned} \langle P \rangle &= \int_0^{\psi_B} P \frac{d\psi}{\psi_B} = \frac{P_0}{\psi_B}\int_0^{\psi_B} e^{-\psi/\psi_p} d\psi \\ &= \frac{P_0 \psi_P}{\psi_B}\left[1 - e^{-\psi_B/\psi_P}\right] \end{aligned} \tag{26}$$

$$\langle \rho \rangle = \frac{\rho_0 \psi_P}{\psi_B}\left[1 - e^{-\psi_B/\psi_P}\right] \tag{27}$$

$$\begin{aligned} \langle Q \rangle &= \int_0^{\psi_B} B^2 \frac{d\psi}{\psi_B} = \int_0^{\psi_B} (B_V^2 - 2P)\frac{d\psi}{\psi_B} \\ &= B_V^2 - 2P_0 \frac{\psi_P}{\psi_B}\left[1 - e^{-\psi_B/\psi^P}\right] \end{aligned} \tag{28}$$

We consider configuration ii) with mirror ratio 4, and describe the code output with Fig. 5: figure 5a gives the field-line 2.5 cm off the axis at M_{01} ; Fig. 5b gives mod-B along the field-line; Fig. 5c gives the eccentricity of the flux surface; Fig. 5d gives the line-bending coefficient L: Fig. 5e gives the driving coefficient D; Fig. 5f gives the inertia coefficient I; Fig. 5g and h give the eigenfunction and its derivative, respectively; Fig. 5i and j give the stability function (line-bending plus driving energy) and its integrated value with respect to z, respectively; Fig. 5k and l give, separately, the line-bending and driving energy, respectively. Here, we see that the system's stability is determined by the balance between

the line-bending and driving energy, that is represented by the sign of the integral of the stability function (+ for stability).

If we consider stability only for the mirror confined regions, the eigenvalues with $\beta = 0.01\%$ are -6.007×10^{8} for the configuration ii) with mirror ratio 3 and reduced quadrupole current, -1.908×10^{9} for the configuration iii) with mirror ratio 4 and full quadrupole current, and -4.436×10^{9} for the configuration iii) with mirror ratio 3 and reduced quadrupole current. These results imply that the mirror confined region is flute unstable whereas the experimental data show that the system is flute stable. We observe that the long solenoid regions outside the mirror confined region enhance stability by providing large inertia and line-bending energy, and the diverging field regions near the end of the machine enhance stability by providing very strong good driving curvature regions. So, we consider the bllooning stability over the entire machine. We assume that the temperature is constant and the density varies with the field intensity in such a manner that the value of β is maintained constant in the diverging end-field regions, and that the pressure is maintained constant at all intermediate axial locations, in rough agreement with experimental observations.

With the good curvature in the end regions included, all experimental configuration satisfy the flute stability criterion; $\delta\int\frac{dl}{B}>0$. Since the plasma pressure is assumed to fall off with B^2 at the ends, neither fixed nor floating boundary condition calculations are sensitive to the exact locations of the initial and final points of the integration. The calculations yield values of β_c within a few percent of each other (with the fixed exceeding the floating end values).

The results for each of the four configurations studied experimentally are given as follows.

Configuration (i): With the multiple-mirror fields that are theoretically stable to flutes at low β, the rigid mode ballooning code predicts stability for all

β's up to and beyond the validity of the code. With smaller weak quadrupole current the ballooning code predicts instability at essentially the same value of the stabilizing current as predicted by the flute unstable result found from the code MAFCO [12], for all values of β. There is no significant mode amplitude ratio between stable and unstable regions at any β, indicating that finite β ballooning effects are not important for this configuration. These results are in agreement with the experimental observations.

Configuration ii); the calculated transition to instability is found to be high, giving β_c = 55% for the rigid mode (β_c = 22% for the high-m mode). The experimentally observed critical beta is $\beta \geq 15\%$. Figure 6a-d are code output with β_c = 55%. Figure 6a is a plot of the eigenfunction with floating boundary conditions. Figure 6b and c are the line-bending energy and the driving energy, respectively. Figure 6d is the stability function. From Fig. 6b, we observe the relatively strong contribution of the solenoid regions to the line-bending energy. From Fig. 6c, we observe that relatively strong bad curvature regions are concentrated near T_0 and T_4, and strong good curvature regions near the end of the machine, M_{12}, and near the transition to the solenoid after T_5. From Fig. 6a we osbserve that the mode amplitude is maximum near M_{34}, which is near the center of bad curvature between the two bounding good curvature regions.

Configuration iii): The calculated transition to instability occurs at β_c = 10% for the rigid mode (β_c = 4% for high-m mode) for mirror ratio 3 and 80% reduced quadrupole current. For the same configuration with mirror ratio 4 and full quadrupole currents, ballooning occurs at β_c = 23% for rigid mode (β_c = 7% for high-m mode). These values are contrasted with experimentally observed critical betas of $\beta \geq 10\%$ and $\beta \geq 5\%$ respectively. Figure 7a-d are code output with β = 8%. Here we observe that relatively strong bad curvature regions are nearly uniformly distributed from the transition to the solenoid

before T_0 to T_5, and there are very strong bad curvature regions near T_2. Strong good curvature regions are M_{12}, near T_3, the transition to the solenoid after T_5, and the diverging field regions at the ends of the machine. We also observe that the mode amplitude has a broad maximum near the main bad curvature regions (T_2).

Configuration (iv): For this configuration, the symmetry between the 0° and 90° field lines is broken, making the analysis of this configuration quite complicated. Specifically the 90° field line is flute unstable. The 0° field line possesses very little bad curvature and is flute stable. For the rigid mode, this configuration is unstable. The high mode calculation along the 0° line predicts β_c = 26%. Experimentally no ballooning activity was observed for minor ratio 3; for mirror ratio 4 ballooning is observed for $\beta \geq 10\%$; and for mirror ratio 5 ballooning occurs at $\beta \geq 7.5\%$.

The measured values of β and the theoretical values of β_c for each configuration are summarized in Table I.

Figure 8 is a plot of the eigenvalue versus beta for configuration (iii) with mirror ratio 4 and full quadrupole. The eigenvalue saturates at approximately $\pm 3.0\times10^{9}\text{sec}^{-2}$, + for higher betas and - for lower betas. This plot shows that the growth rate of the ballooning instability changes quite abruptly near the critical beta.

The effect of the pressure profile on the eigenvalue is summarized in Table 2. Here, we take a magnetic field configuration which has mirror ratio 4, no weak quadrupole between M_{12} and M_{34}, optimized quadrupoles for the other parts of mirror regions, and solenoid regions with diverging end-field at the ends of the machine. As a reference profile, we take a uniform pressure profile except at the diverging end-field regions where pressure is proportional to β^2. For the profiles 2-5, pressure is either increased or decreased uniformly over

the solenoid regions that have neutral driving effect on the average. For the profiles 6-9, pressure is either increased or decreased uniformly over the regions 50 cm to 280 cm (M_{12}) and 420 cm (M_{34}) to 870 cm, that have good driving effect on the average. For profiles 10-11 the relative pressure at the beginning of the diverging field region is either increased or decreased.

We observe that the critical betas are slightly reduced ($\Delta\beta_c < 2\%$) for all the profiles except the profiles 4 and 8. These results can be explained qualitatively by observing Eq. (25). We multiply Eq. (25) by u and integrate along the field line to obtain

$$\omega^2 = \frac{\int_{-l}^{l} dz \left[\mathrm{L} \left(\frac{du}{dz} \right)^2 - Du^2 \right]}{\int_{-l}^{l} dz\, Iu^2} \tag{24'}$$

The difference in eigenvalues between the reference and the pressure weighted profile becomes

$$\omega_1^2 - \omega_2^2 = \omega_1^2 \left(\frac{\Delta E_I}{E_I + \Delta E_I} \right) - \frac{\Delta(E_L + E_D)}{E_I + \Delta E_I}$$

where ω_1^2 and ω_2^2 are the eigenvalues for the reference and the pressure weighted profiles, respectively, $E_L \equiv \int_{-l}^{l} dz\, \mathrm{L} \left(\frac{du}{dz} \right)^2$ is the line-bending energy, $E_D \equiv \int_{-l}^{l} dz\, Du^2$ is the driving energy, and $E_I \equiv \int_{-l}^{l} dz\, Iu^2$ is the inertial energy. Since we are studying the pressure weighting effects near marginal stability, we set $\omega_1^2 = 0$, and we have

$$\omega_2^2 = \frac{\Delta(E_L + E_D)}{E_I + \nabla E_I} \tag{29}$$

Since $\sigma'' = 0$ on the average for the solenoid region, $\Delta E_D = 0$ for profiles 2-5 (for profiles 6-9, the pressure also changes in good curvature regions but the mode amplitude changes in the opposite direction due to the change in inertia, so

partially cancelling the effect). From the definition of L as given for Eq. (25) we see that L is independent of pressure if the pressure is isotropic, as assumed here. Therefore if we neglect the variartions in the eigenfunction, such that $\frac{du}{dz}$ does not change, then $\Delta E_L = 0$. We see, then, from (29) that ω_2^2 is zero, implying no change in the β_c of the mirror confined region. Actually, there is a small change in the eigenfunction with pressure wieghting. So, we expect some change in β_c due to $\Delta\left[\frac{du}{dz}\right]^2$. Changing the pressure in the good curvature diverging field region has a marked effect on ballooning stability, as expected.

V. Discussion

We have some differences between the theoretically calculated values and the experimental observations of the critical betas β_c. The calculated values of β_c for the rigid mode are higher than the experimental values, except for the configuration (iv) for which the system is flute unstable in theory. Higher predicted β_c may be accounted for by the effects not included in analysis, e.g., resistive effects and the breakdown of the paraxial approximation in the diverging field region. Resistivity can partially decouple the driving bad curvature and anchoring good curvature regions. Instabilities can then exist at values of β below the ideal MHD critical β since the plasma can slip across the field without bending the lines, thereby reducing the restoring forces. The additional decoupling of the driving regions from the large inertia on the long connecting regions is expected to result in increased growth rate. An estimate of the effect of resistivity for the experimental parameters indicates that this effect is significant [1]. In the dierging end-field region, our calculated curvature from the paraxial approximation is probably over-emphasized, giving higher critical betas.

The reversal of the calculated critical betas in configuration (iii), for the mirror ratio 3 reduced quadrupole case and the mirror ratio 4 full quadrupole

case, and the fact that the configuration (iv) is experimentally flute stable are anomalies that have not been explained.

Detailed axial variations of pressure that may exist in the experiment have not been included in the computed values of β_c presented in Table 1. However, parametric numerical studies of pressure variations in various sections of the device demonstrate that β_c is not sensitive to axial pressure variations in the solenoid but is sensitive to pressure variations in the diverging field regions. These studies indicate that the small deviations of the actual profile from the assumed flat profile can only make commensurately small changes in the predicted values of β_c.

In conclusion, the rigid mode ballooning calculation predicts higher critical beta than that observed. Resistive corrections and non-rigid low-m corrections to the rigid mode ballooning equation are expected to improve the agreement between the theory and experiment.

Acknowledgements

The author wishes to thank Dr. H. D. Price, Professor A. J. Lichtenberg, and Professor M. A. Lieberman for providing expeirmental data, and for the numerous discussions involving the theoretical aspects of the rigid mode ballooning instabilities. Thanks also go Dr. T. B. Kaiser, Dr. W. M. Nevens, and Dr. L. D. Pearlstein for providing the rigid mode ballooning theory and the high-m ballooning code.

This work was supported by Department of Energy Contract DE-AT0E-76ET53059.

References

[1] H. D. Price, N. M. P. Benjamin, B. K. Kang, A. J. Lichtenberg, and M. A. Lieberman, submitted to Phys. Fluids.

[2] W. A. Newcomb, *J. Plasma Physics 26*, 529 (1981).

[3] T. B. Kaiser, W. M. Nevins, and L. D. Pearlstein, *Phys. Fluids 26*, 351 (1983).

[4] W. M. Nevins and L. D. Pearlstein, Physics Basis for an Axicell Design for the End Plugs of MFTF-B (D. E. Baldwin and B. G. Logan, eds.), Lawrence Livermore National Laboratory Report UCID-19359 (1982).

[5] D. A. D'Ippolito and B. Hafiz, *Phys. Fluids 24*, 2274 (1981).

[6] D. A. D'Ippolito, G. L. Francis, J. R. Myra, and W. M. Tang, *Phys. Fluids 24*, 2270 (1981).

[7] T. B. Kaiser, Physics Basis for MFTF-B (D. E. Baldwin et al. ed.), Lawrence Liermore National Laboratory Report UCID-18496, Section IV-B.

[8] G. G. Vandergrift, Ph.D. Thesis, Dept. of Physics, University of California, Berkeley, 1982.

[9] L. D. Pearlstein, T. B. Kaiser, and W. A. Newcomb, *Phys. Fluids 24*, 1326 (1981).

[10] H.D. Price, Ph.D. Thesis, Dept. of Nuclear Engineering, University of Califonria, Berkeley, 1983.

[11] J. C. Riordan, A. J. Lichtenberg, and M. A. Lieberman, *Nucl. Fusion 19*, 21 (2979).

[12] W. A. Perkins and J. C. Brown, Lawrence Livermore National Laboratory Report UCRL-7744-Rev. II (1966).

TABLE I. Summary of Configurations, Experimental and Theoretical β_c (percent)

Configuration Description	Experiment	Theory	
		m = 1	m = ∞
(i) Standard fields	stable (> 25)	-	-
(ii) No quadrupole from $M_{12} - M_{34}$			
T_2 and T_3 off; reduced quad.	15	55	22
(iii) Pulsed off WQ from $M_{12} - M_{34}$			
(a) M = 3; reduced quads	10	10	4
(b) M = 4; full quads	5	23	7
(iv) Pulsed off WQ from $T_1 - T_3$			
(a) M = 4; full quads	10	unstable	unstable (θ=90°)
			26 (θ=0°)

TABLE 2

	pressure profile	β (%)	eigenvalue	average curvature on the pressure weighting region
1	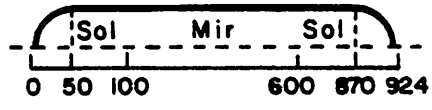	16 17	4.464×10^{7} 3.915×10^{7}	0
2	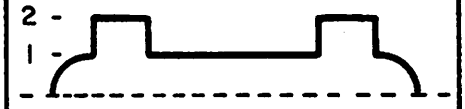	16 17	1.131×10^{7} -5.619×10^{7}	0
3	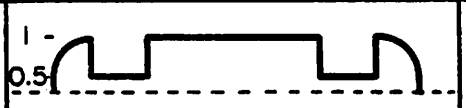	16 17	3.049×10^{7} -6.688×10^{7}	0
4	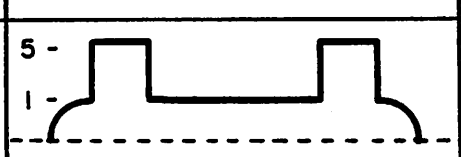	10 11 16	4.955×10^{7} -1.177×10^{7} -3.293×10^{8}	0
5	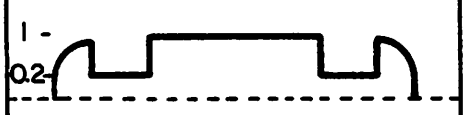	16 17	6.038×10^{6} -1.021×10^{8}	0
6	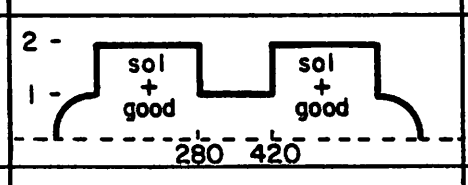	14 15	6.368×10^{7} -3.619×10^{5}	+
7		15 16	5.502×10^{7} -7.686×10^{7}	+
8	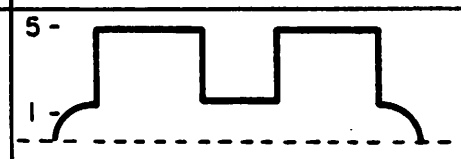	7 8	2.246×10^{7} -6.770×10^{7}	+
9	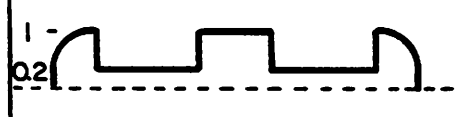	14 15	2.093×10^{7} -1.924×10^{8}	+
10	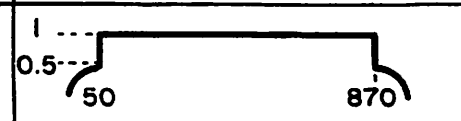	5 10	5.371×10^{7} -2.310×10^{8}	+
11	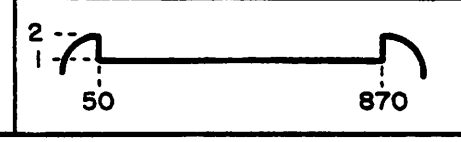	27 30	7.728×10^{6} -2.757×10^{8}	+

Figure Captions

Fig. 1. Fig. 1. The experimental configuration.

Fig. 2. The flux surfaces between mirror throats T_0 and T_5. The mirror and quadrupole currents between M_{12} and M_{34} are removed.

Fig. 3. The flux surfaces between mirror throats T_0 and T_5. The weak quadrupole currents between M_{12} and M_{34} are pulsed off.

Fig. 4. The flux surfaces between mirror throats T_0 and T_5. The weak quadrupole currents between T_1 and T_5 are turned off.

Fig. 5. Ballooning code output; explanation in text.

Fig. 6. Ballooning code output; explanation in text.

Fig. 7. Ballooning code output; explanation in text.

Fig. 8. A typical variation of the eigenvalue with respect to β.

Fig. 9. Ballooning code output; explanation in text.

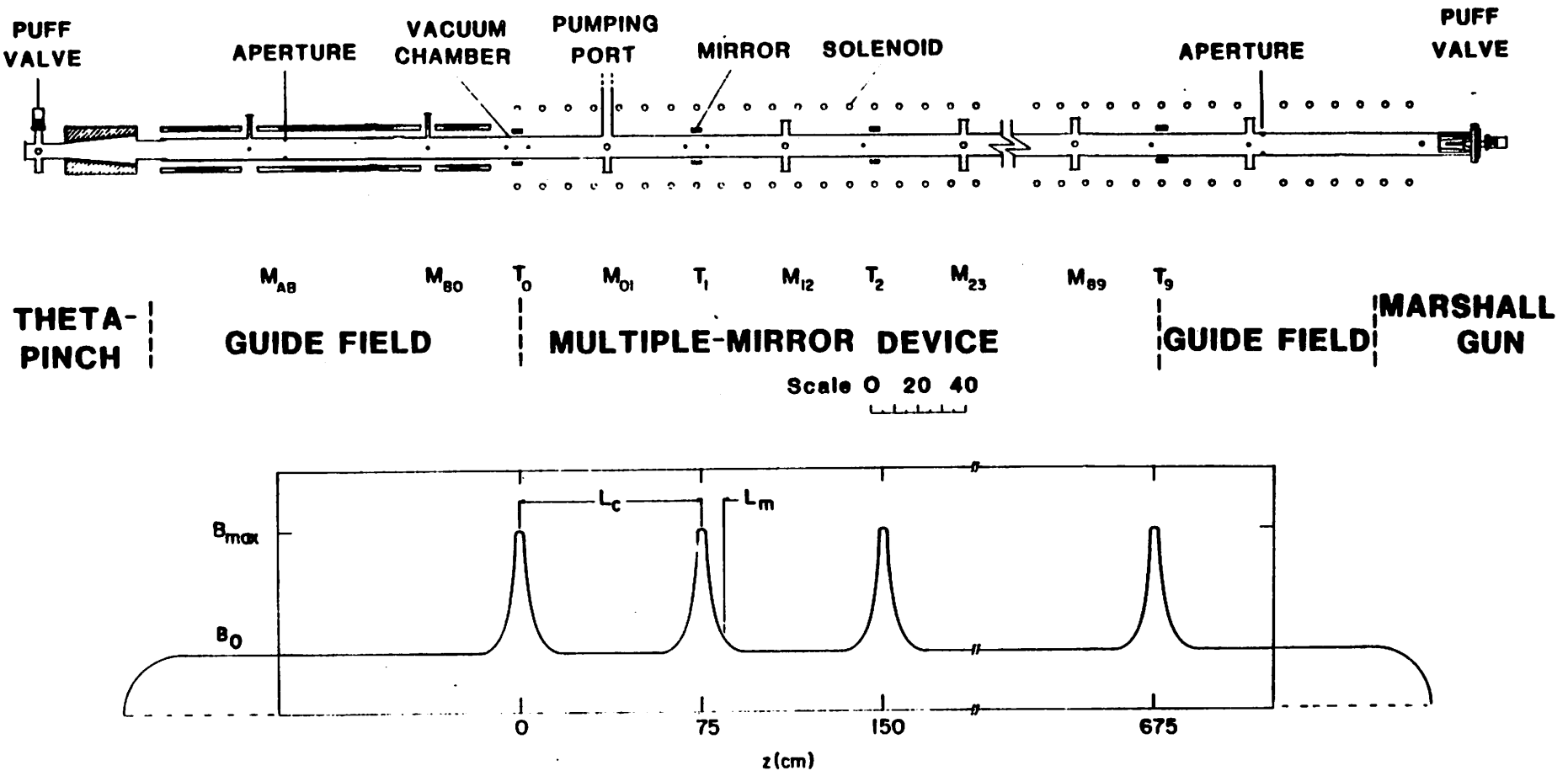
PUFF VALVE
APERTURE
VACUUM CHAMBER
PUMPING PORT
MIRROR
SOLENOID
APERTURE
PUFF VALVE
M_{AB}
M_{80}
T_0
M_{01}
T_1
M_{12}
T_2
M_{23}
M_{89}
T_9
THETA-PINCH
GUIDE FIELD
MULTIPLE-MIRROR DEVICE
GUIDE FIELD
MARSHALL GUN
Scale 0 20 40
L_c
L_m
B_{max}
B_0
0
75
150
675
z(cm)

Fig. 1

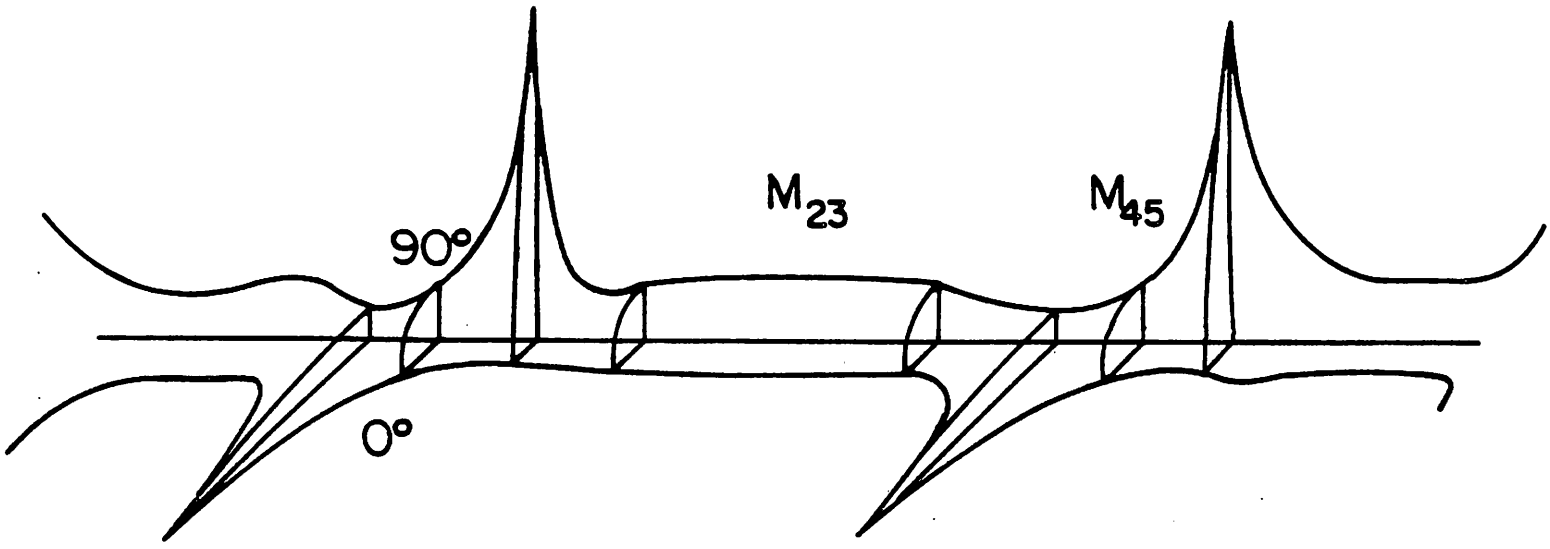

Fig. 2

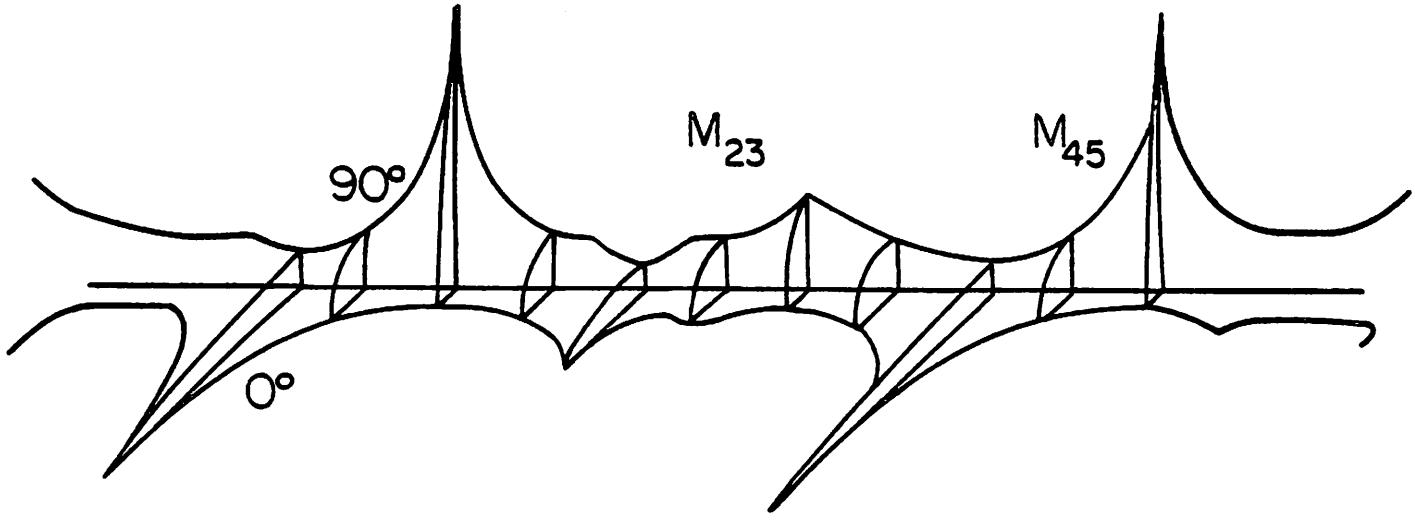

Fig. 3

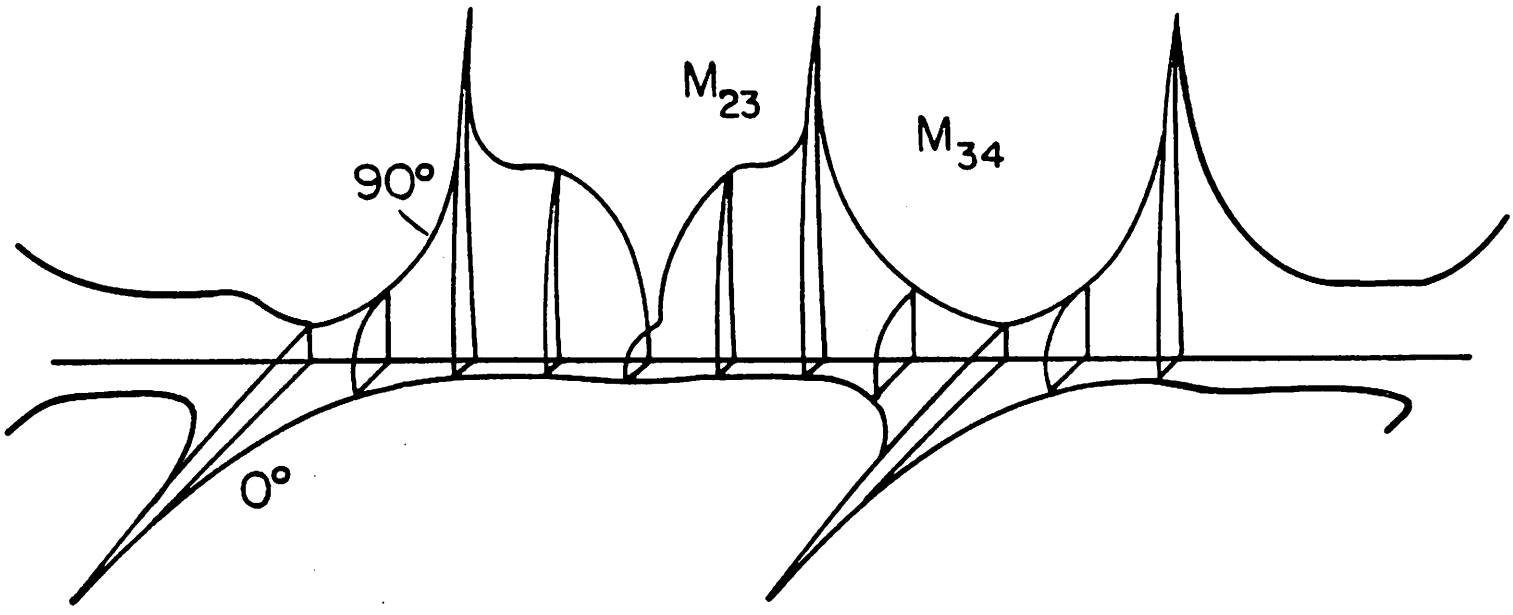

Fig. 4

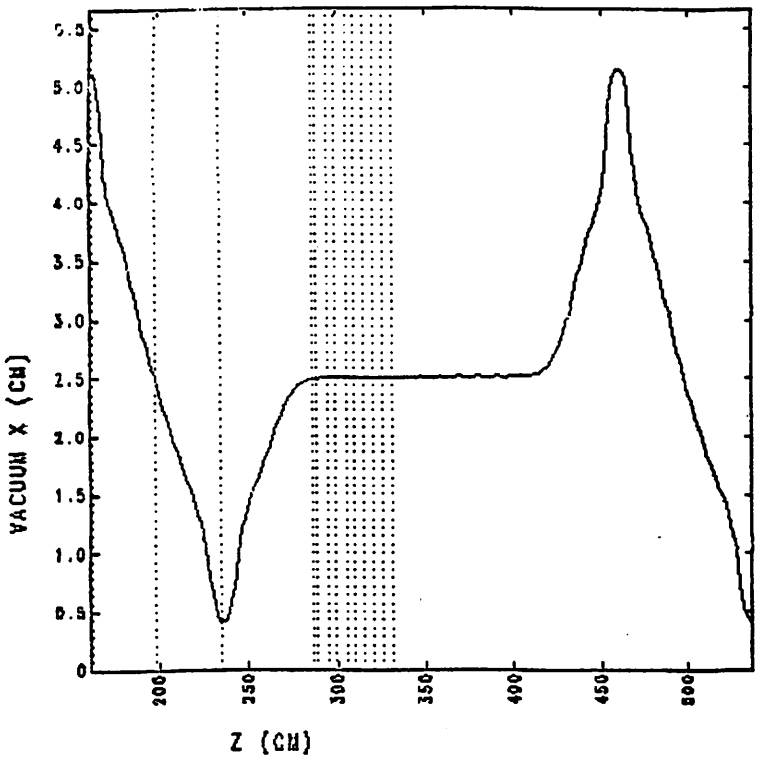
VACUUM X (CM)
Z (CM)

(a)

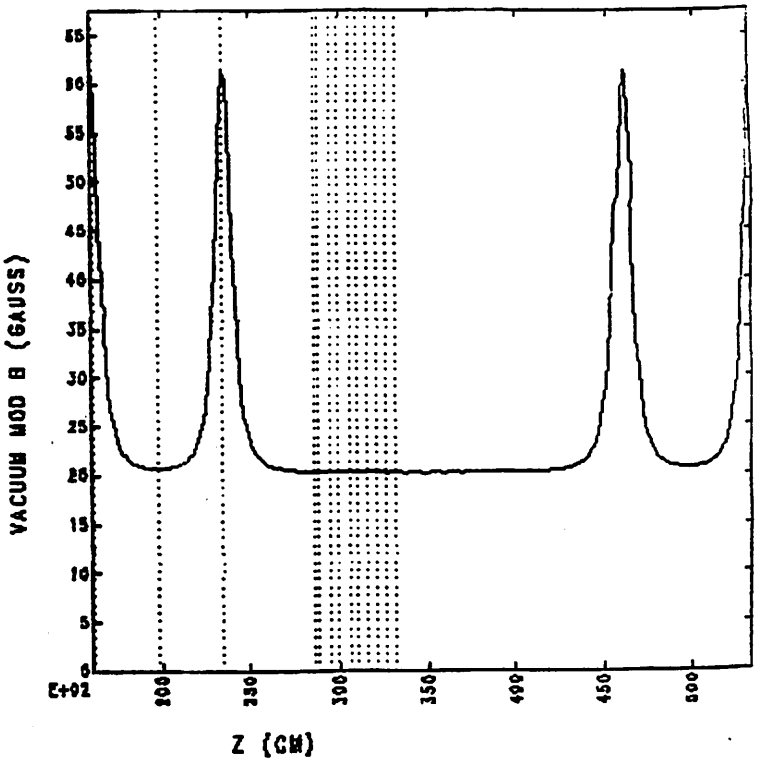
VACUUM MOD B (GAUSS)
E+02
Z (CM)

(b)

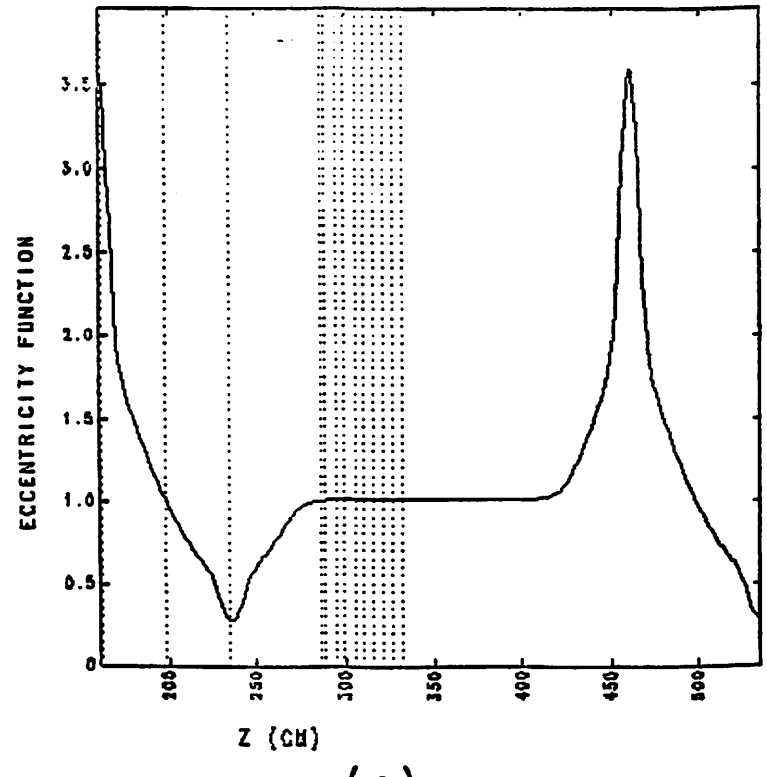
ECCENTRICITY FUNCTION
Z (CM)

(c)

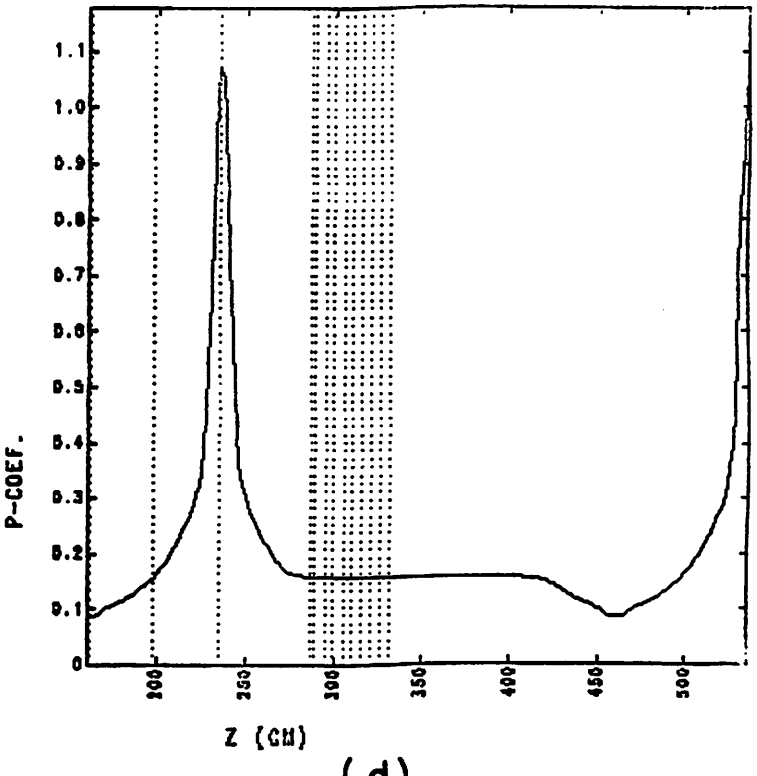
P-COEF.
Z (CM)

(d)

Fig. 5

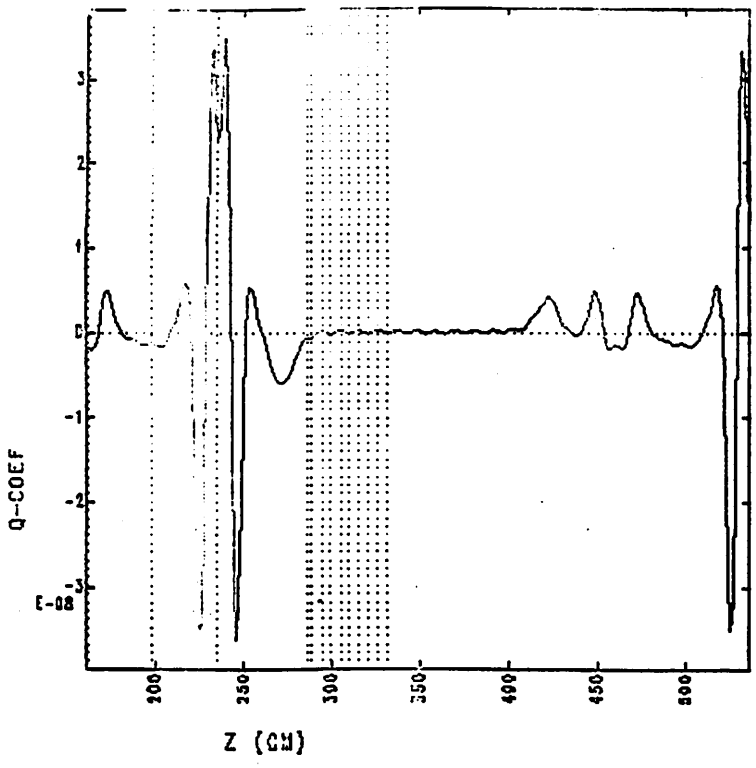
Q-COEF
E-08
Z (CM)

(e)

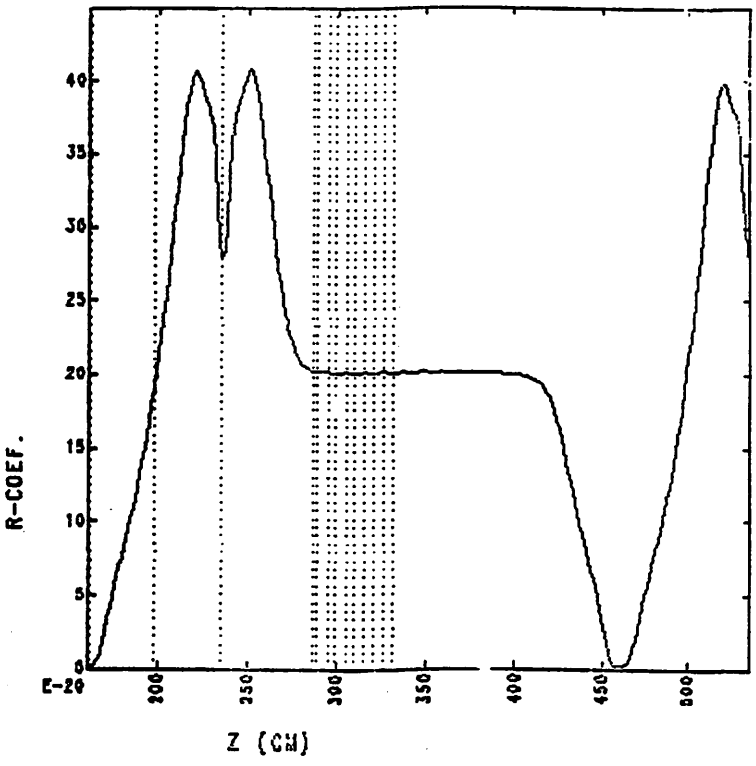
R-COEF.
E-20
Z (CM)

(f)

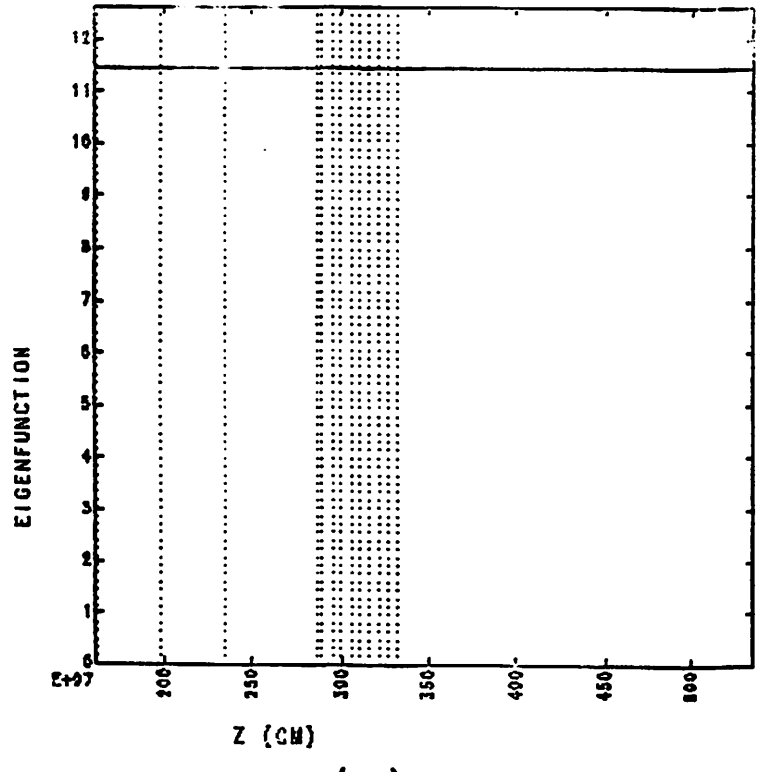
EIGENFUNCTION
E+07
Z (CM)

(g)

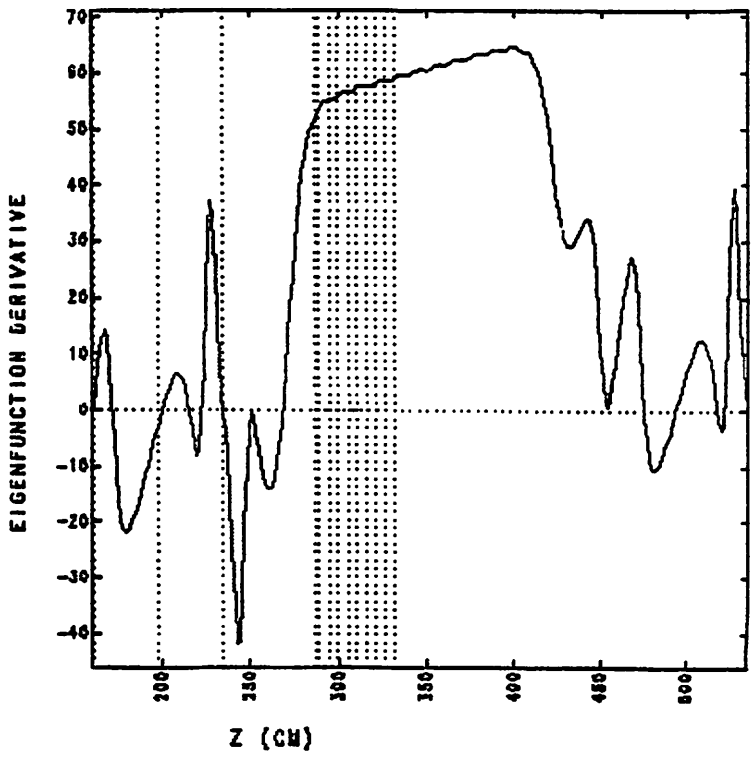
EIGENFUNCTION DERIVATIVE
Z (CM)

(h)

Fig. 5

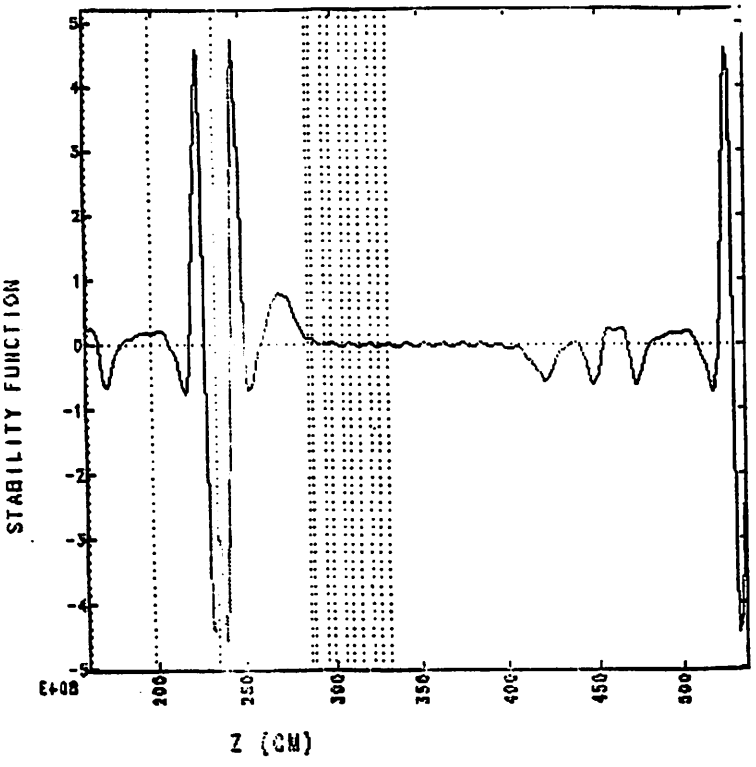
STABILITY FUNCTION
E+00
Z (CM)

(i)

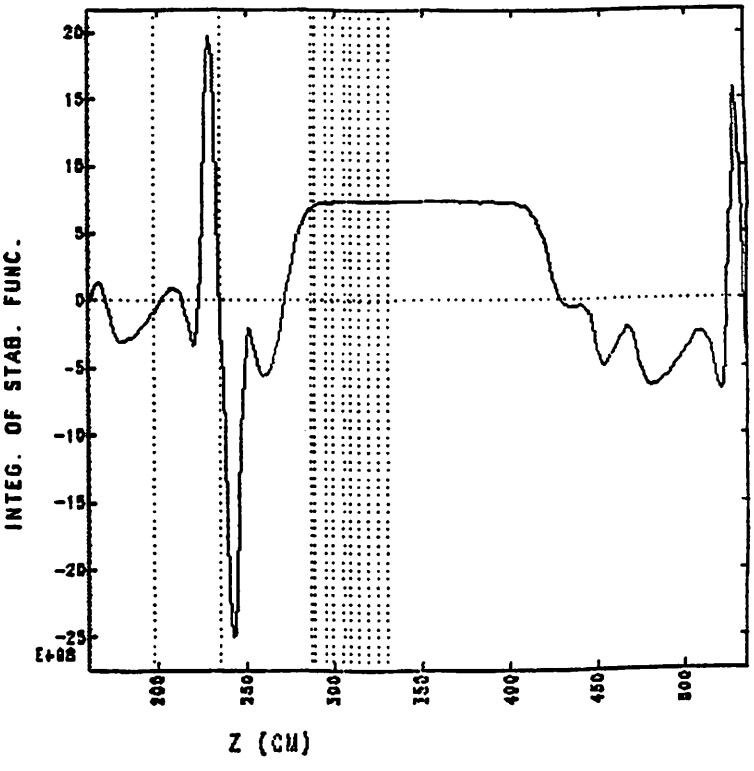
INTEG. OF STAB. FUNC.
E+00
Z (CM)

(j)

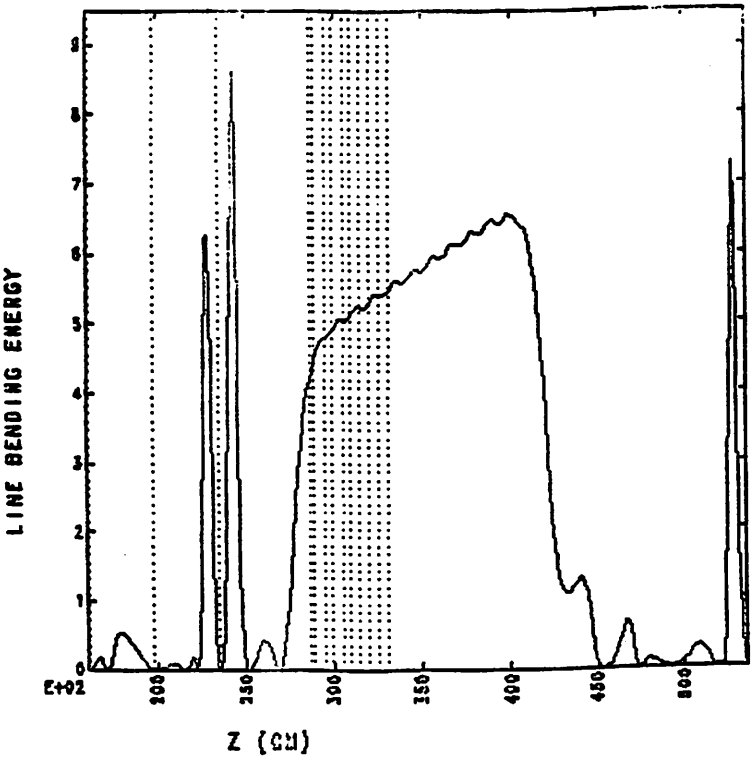
LINE BENDING ENERGY
E+02
Z (CM)

(k)

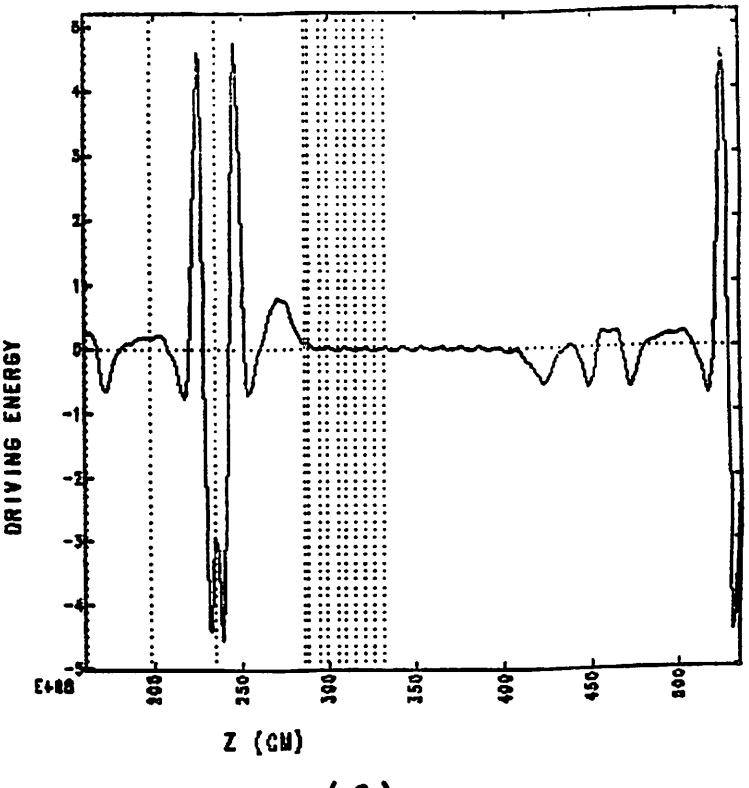
DRIVING ENERGY
E+00
Z (CM)

(ℓ)

Fig. 5

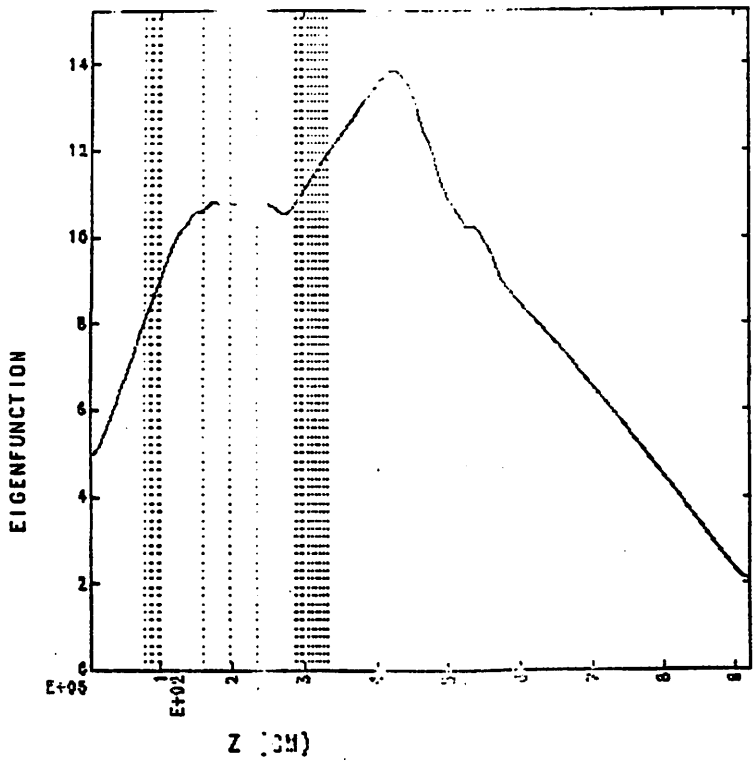
EIGENFUNCTION
E+05
E+02
Z (CM)

(a)

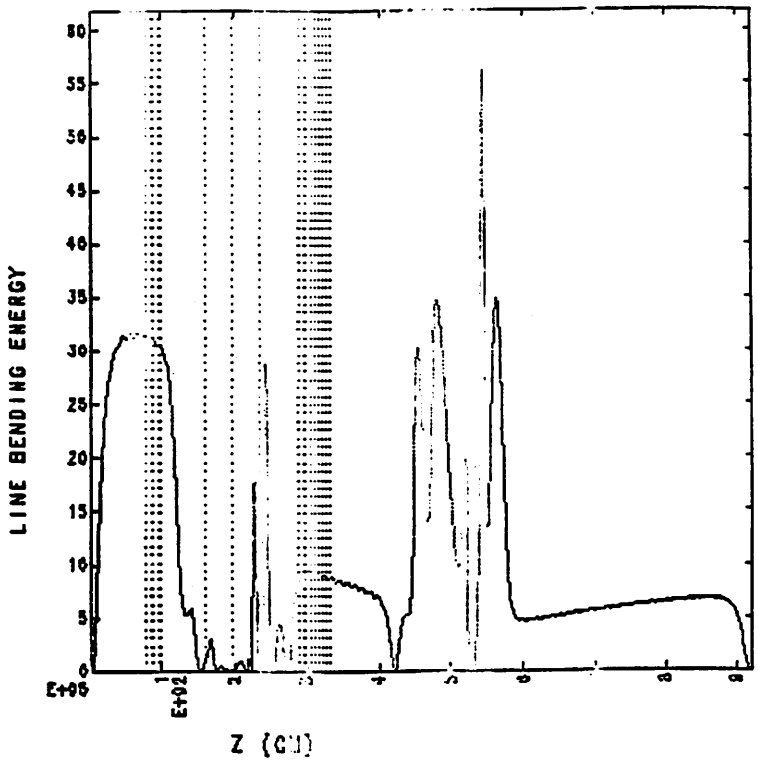
LINE BENDING ENERGY
E+05
E+02
Z (CM)

(b)

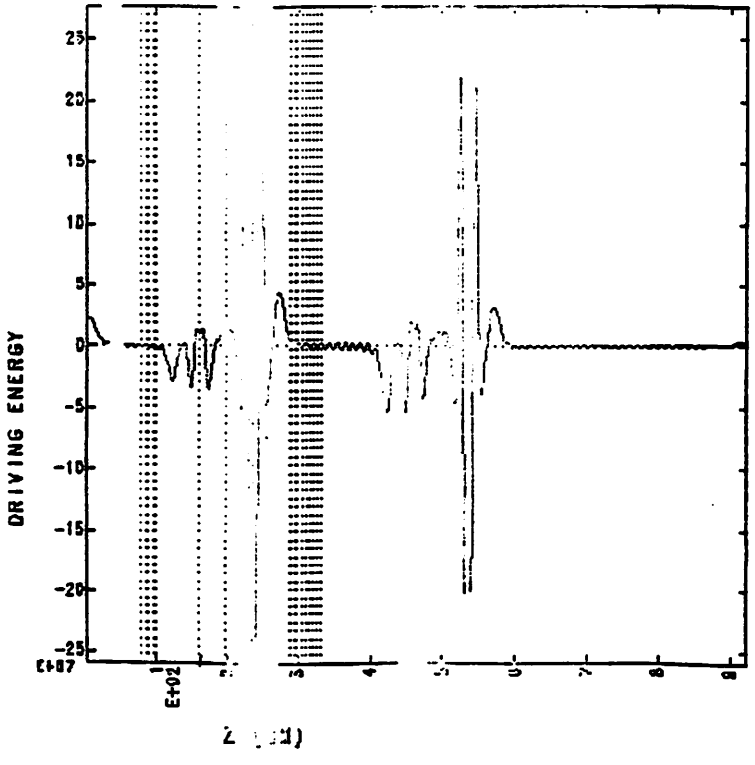
DRIVING ENERGY
E+07
E+02

(c)

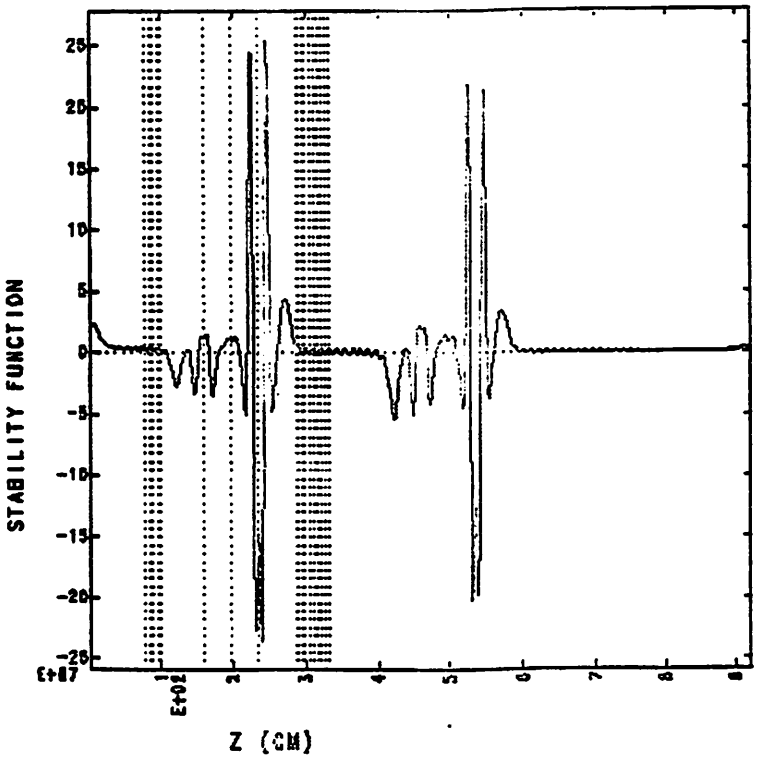
STABILITY FUNCTION
E+07
E+02
Z (CM)

(d)

Fig. 6

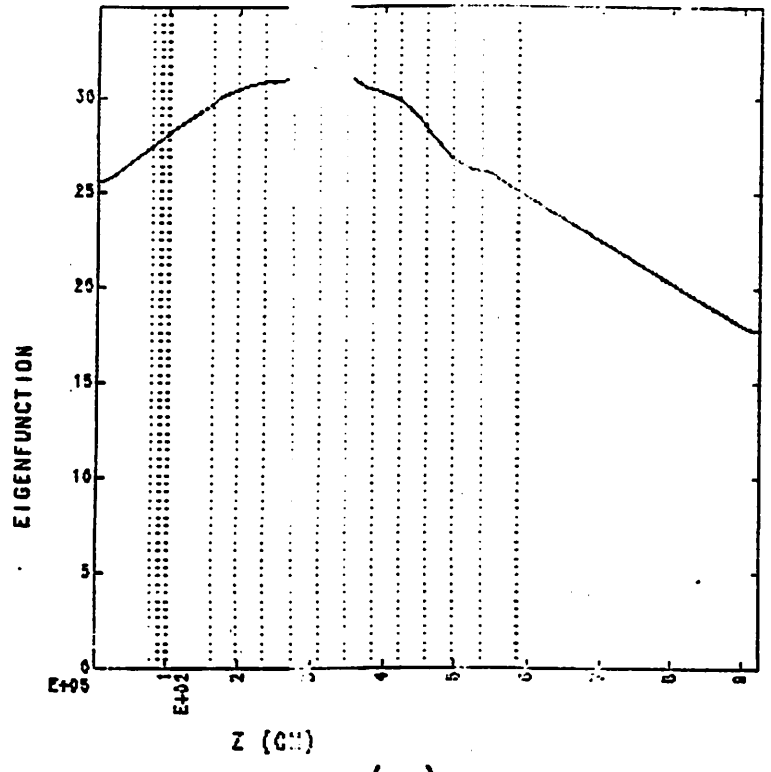
EIGENFUNCTION
Z (CM)

(a)

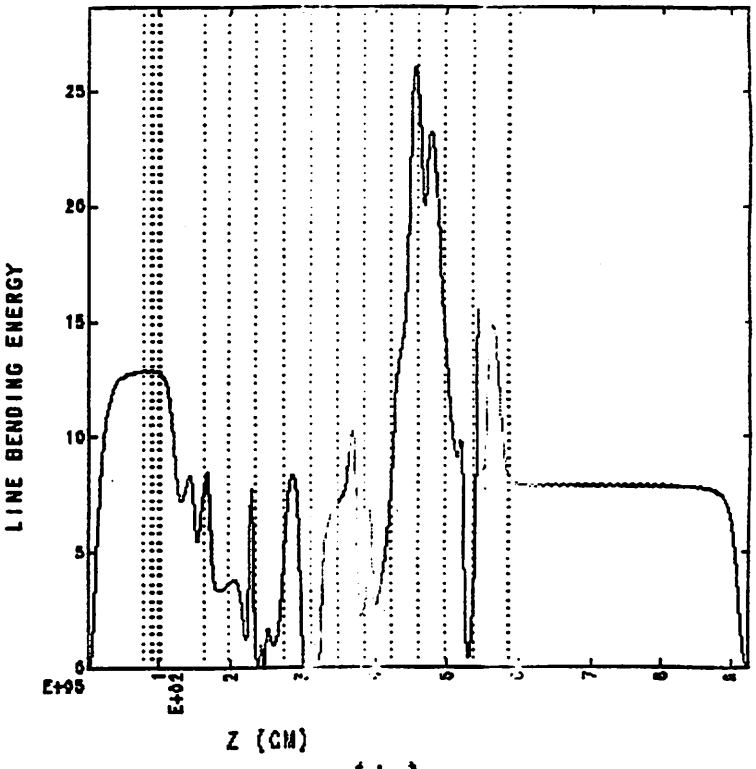
LINE BENDING ENERGY
Z (CM)

(b)

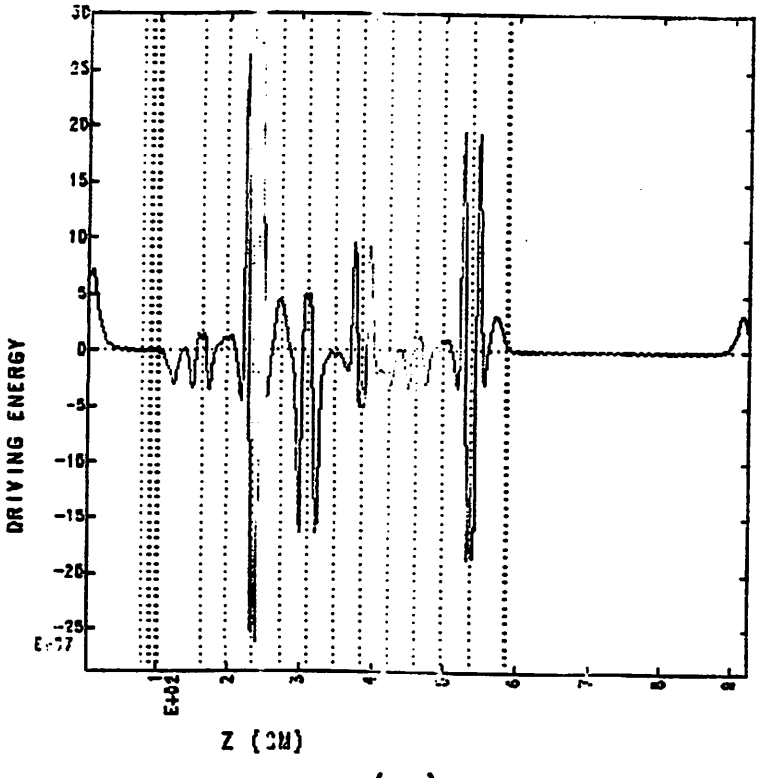
DRIVING ENERGY
Z (CM)

(c)

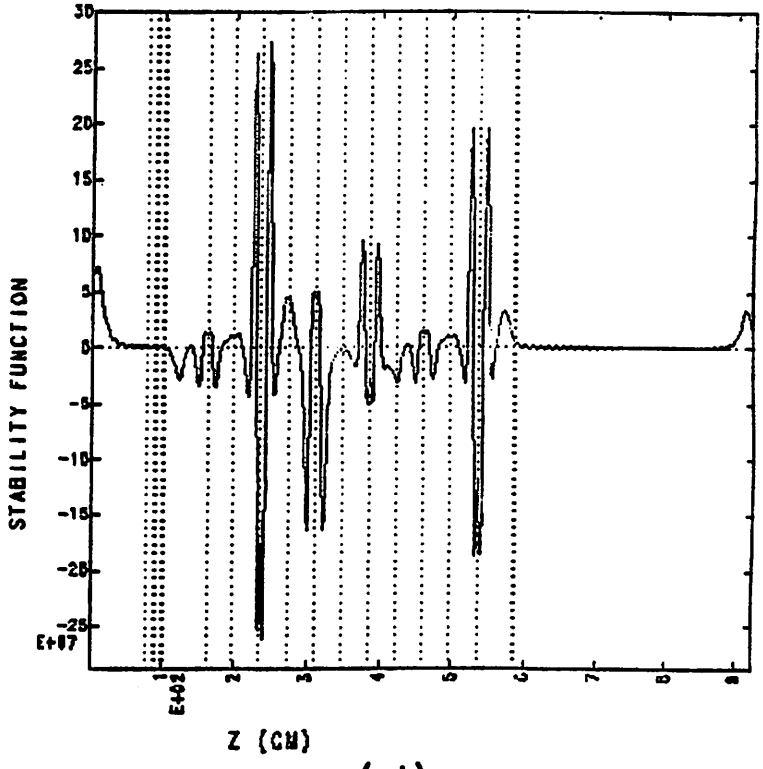
STABILITY FUNCTION
Z (CM)

(d)

Fig.7

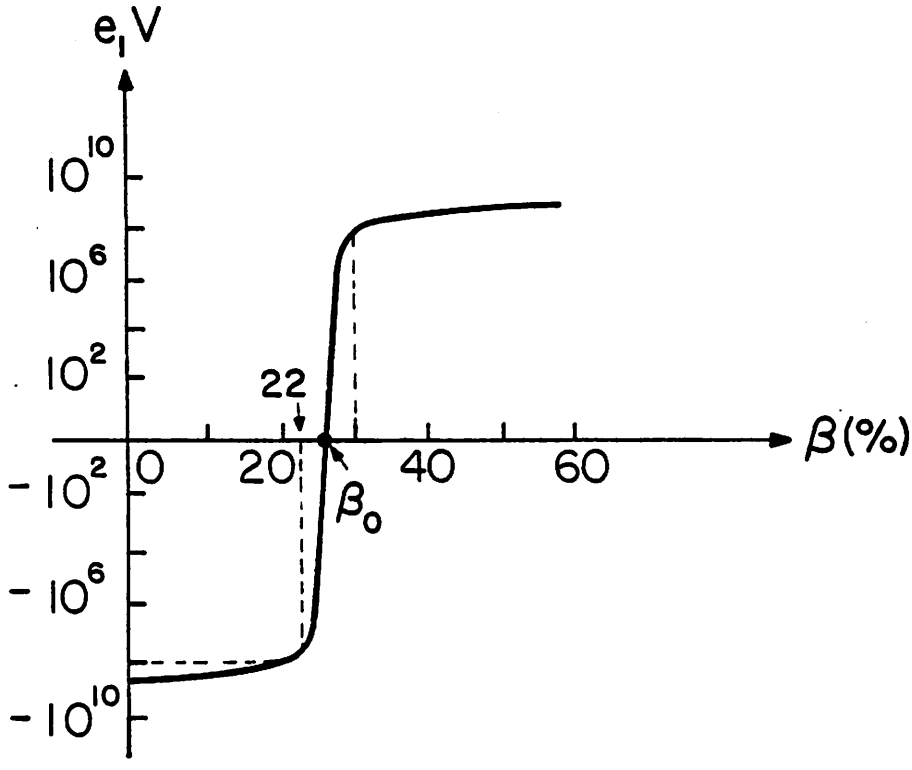

Fig. 8

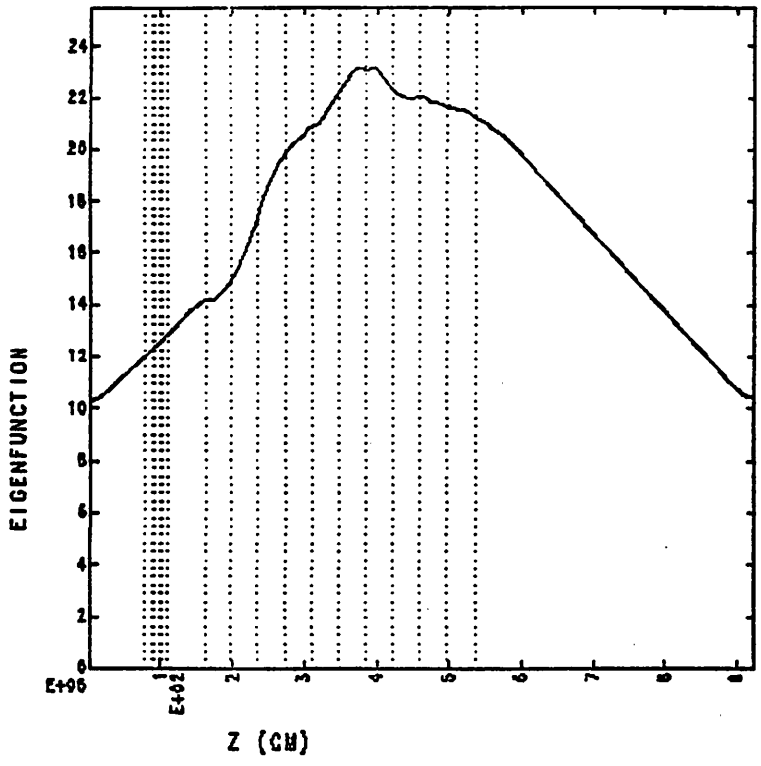
EIGENFUNCTION
Z (CM)

(a)

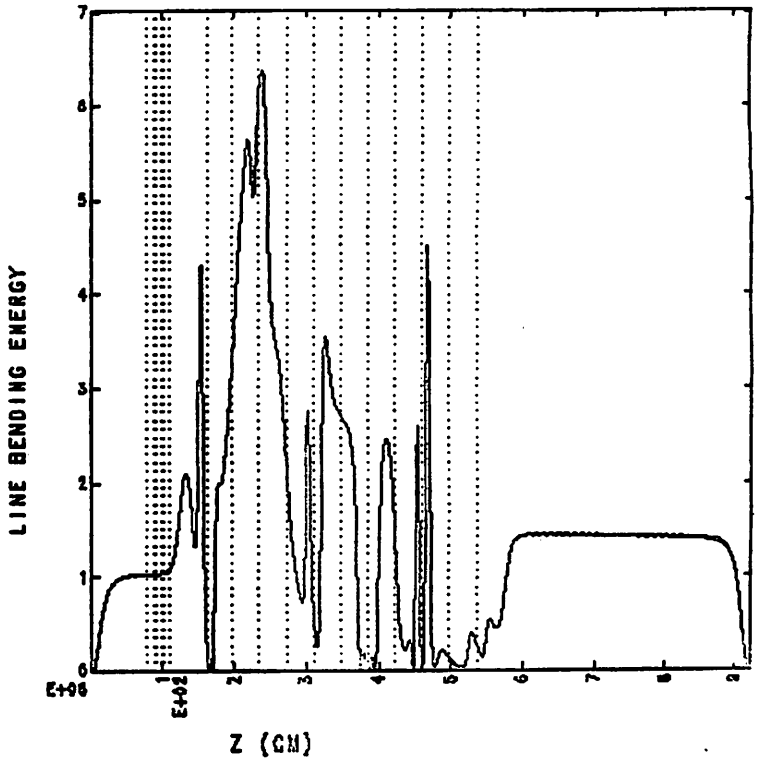
LINE BENDING ENERGY
Z (CM)

(b)

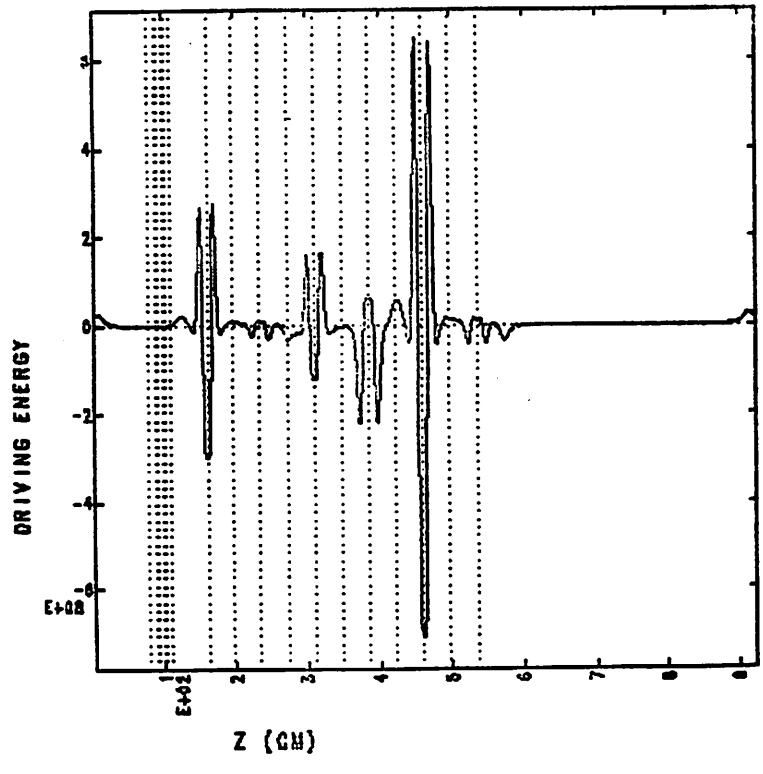
DRIVING ENERGY
Z (CM)

(c)

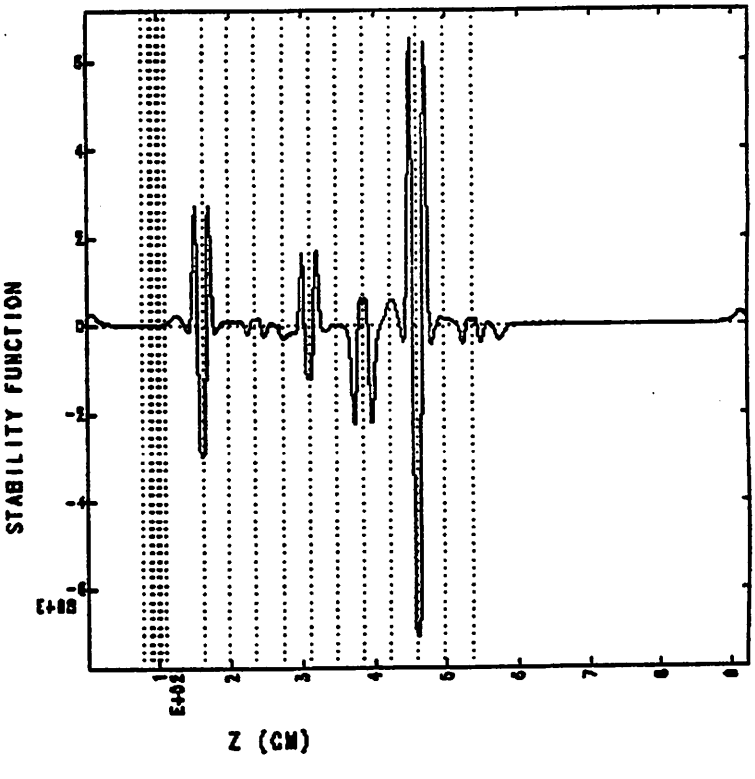
STABILITY FUNCTION
Z (CM)

(d)

Fig. 9

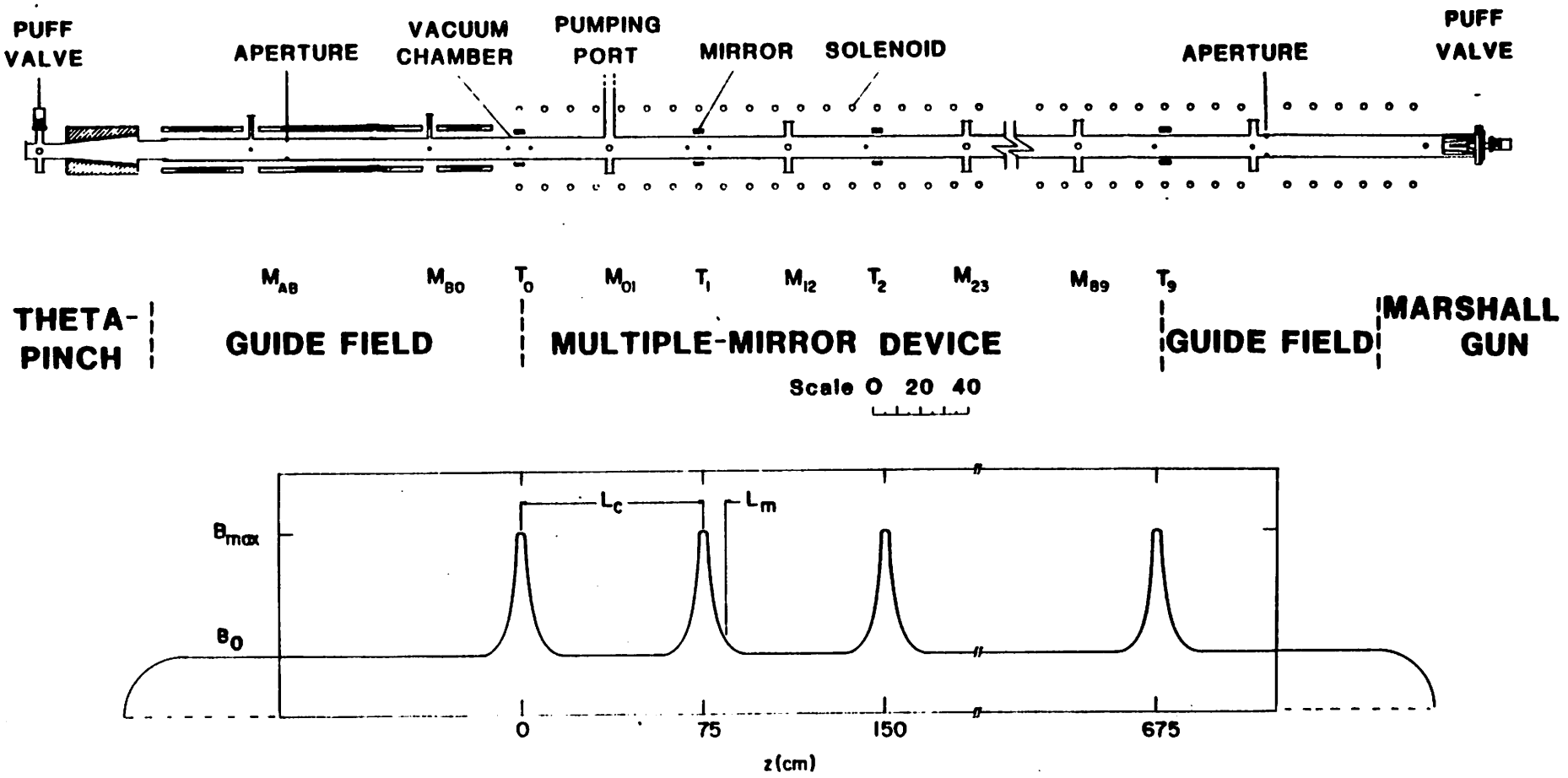
PUFF VALVE
APERTURE
VACUUM CHAMBER
PUMPING PORT
MIRROR
SOLENOID
APERTURE
PUFF VALVE
M_{AB}
M_{80}
T_0
M_{01}
T_1
M_{12}
T_2
M_{23}
M_{89}
T_9
THETA-PINCH
GUIDE FIELD
MULTIPLE-MIRROR DEVICE
GUIDE FIELD
MARSHALL GUN
Scale 0 20 40
L_c
L_m
B_{max}
B_0
0
75
150
675
z(cm)

Fig. 1

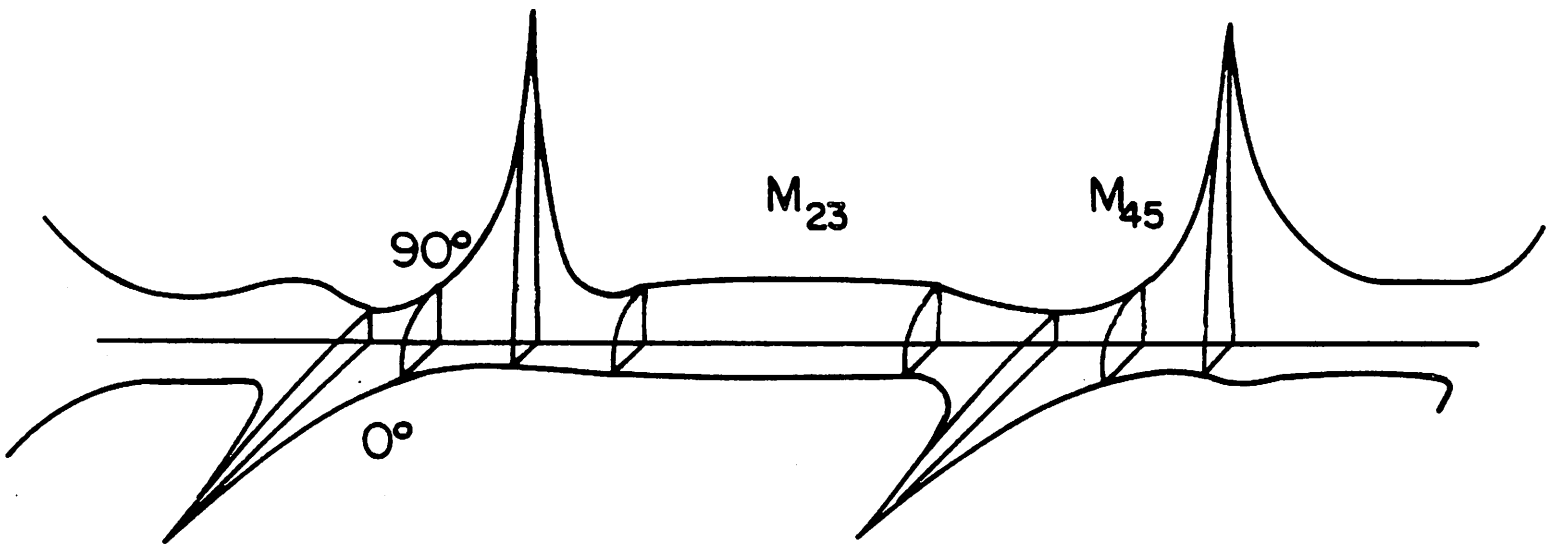

Fig. 2

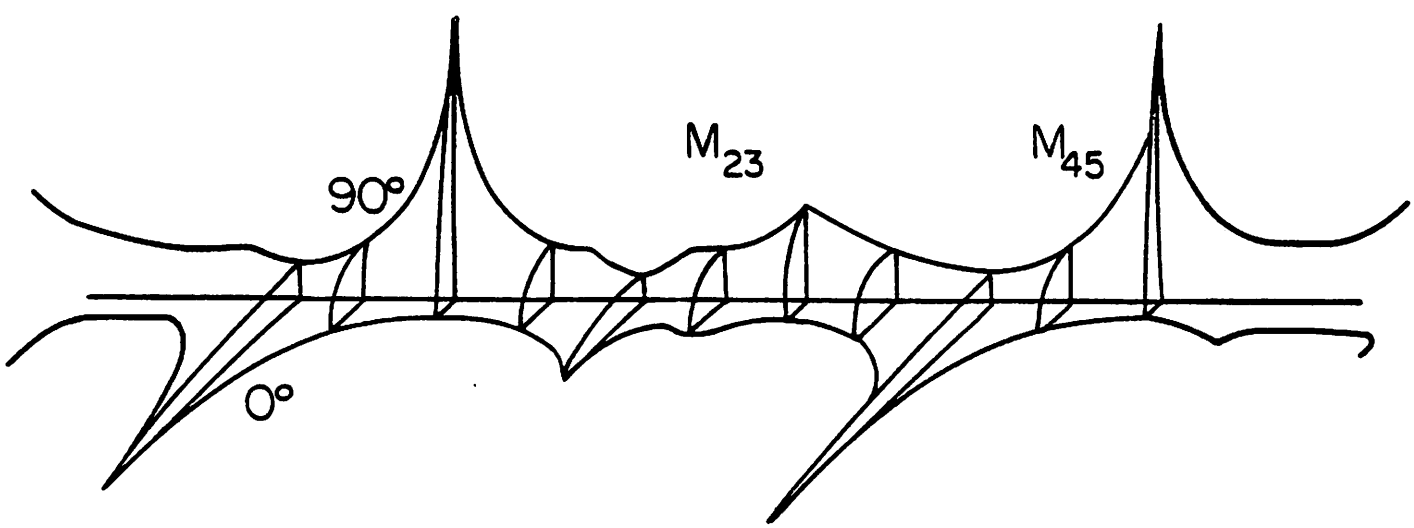

Fig. 3

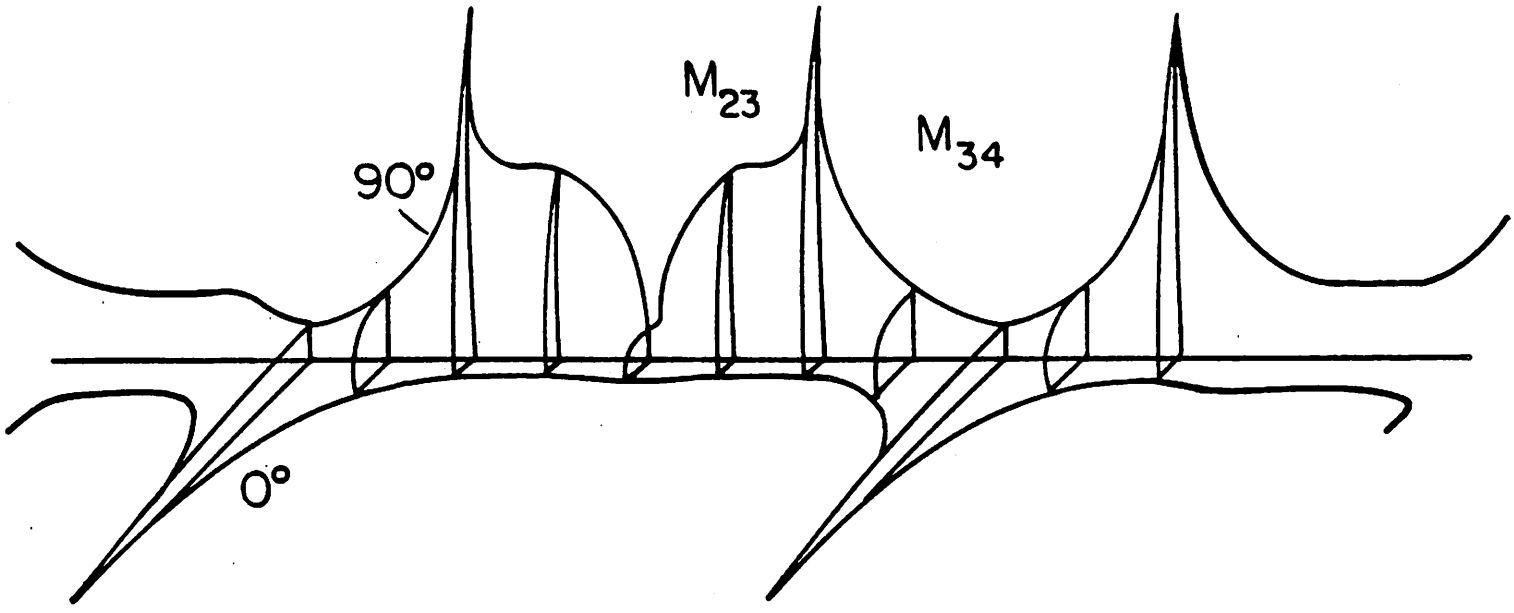

Fig. 4

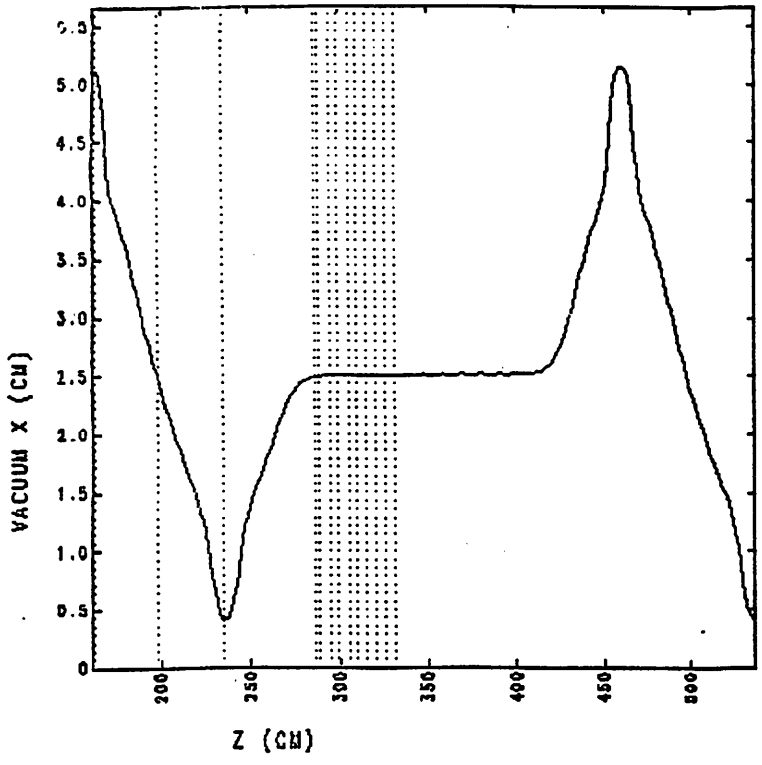
VACUUM X (CM)
Z (CM)

(a)

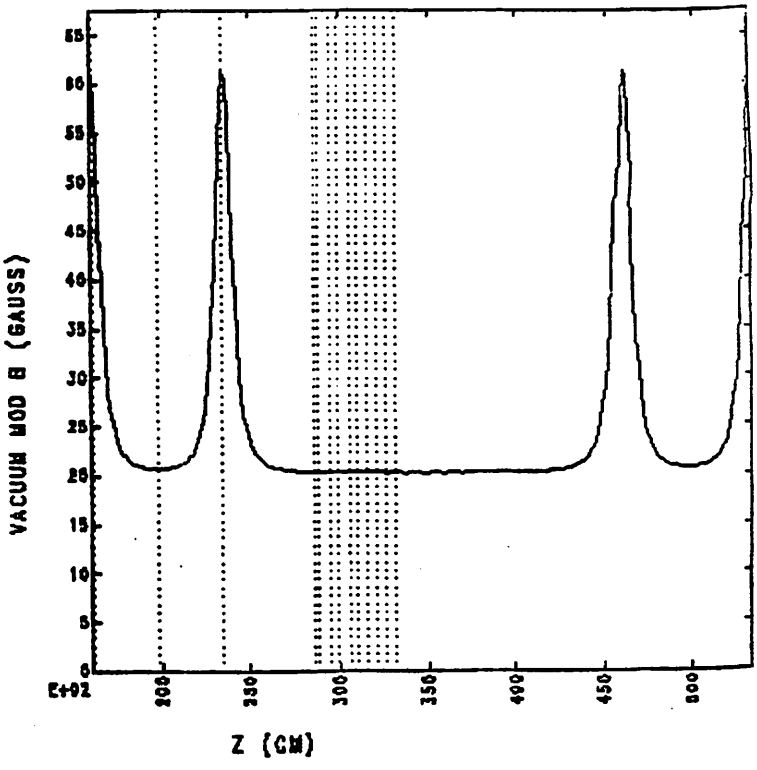
VACUUM MOD B (GAUSS)
E+02
Z (CM)

(b)

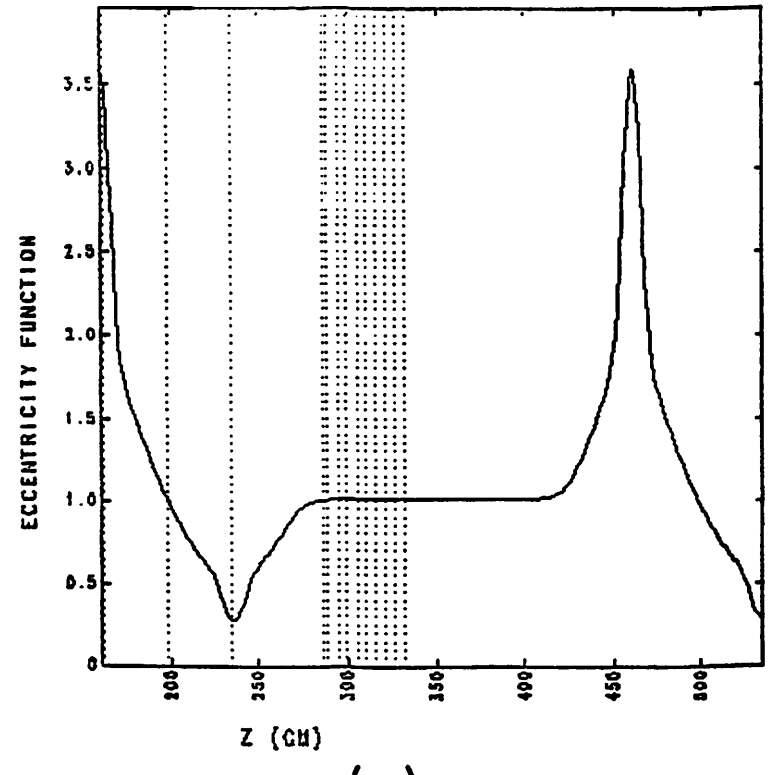
ECCENTRICITY FUNCTION
Z (CM)

(c)

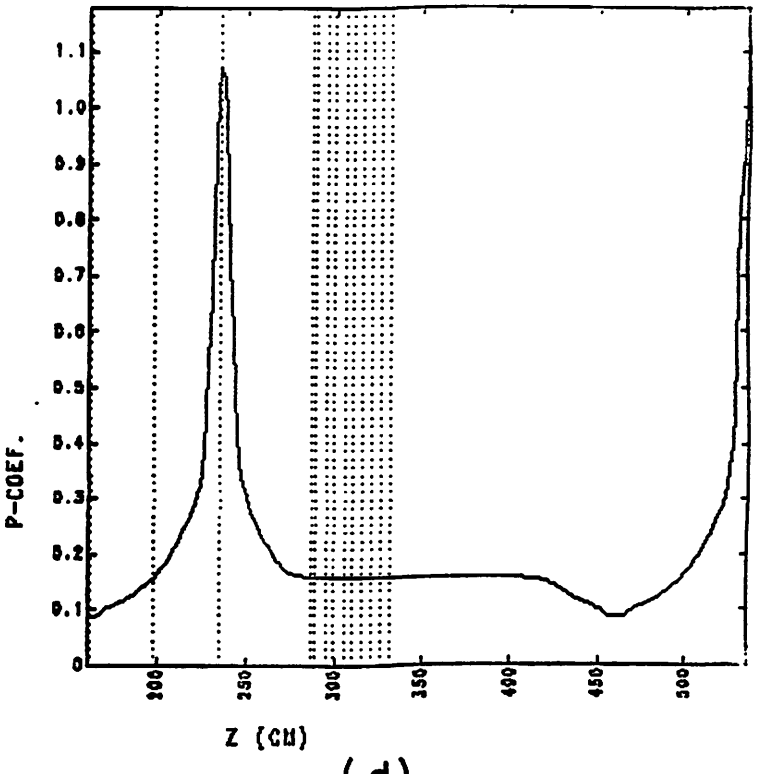
P-COEF.
Z (CM)

(d)

Fig. 5

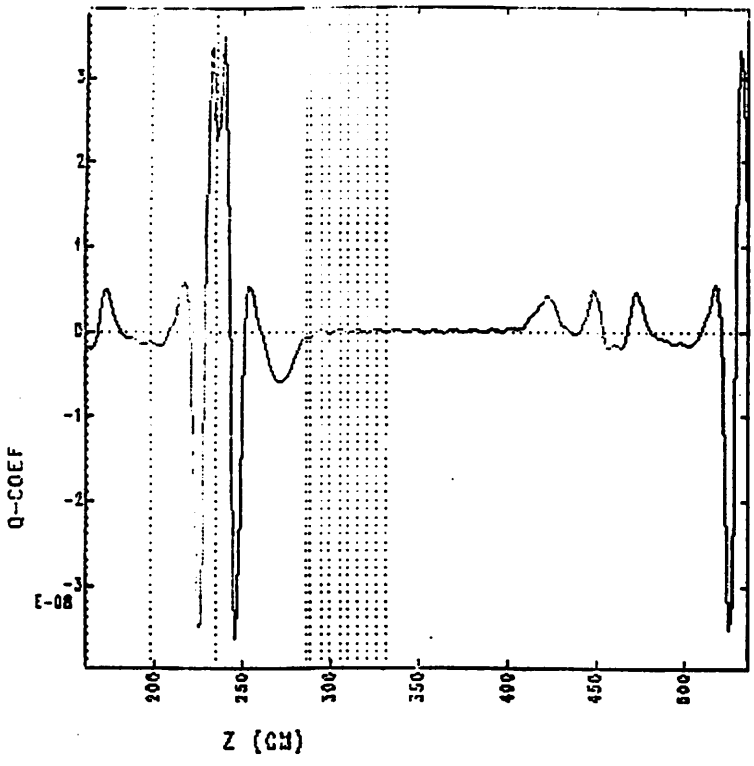
Q-COEF
E-08
Z (CM)

(e)

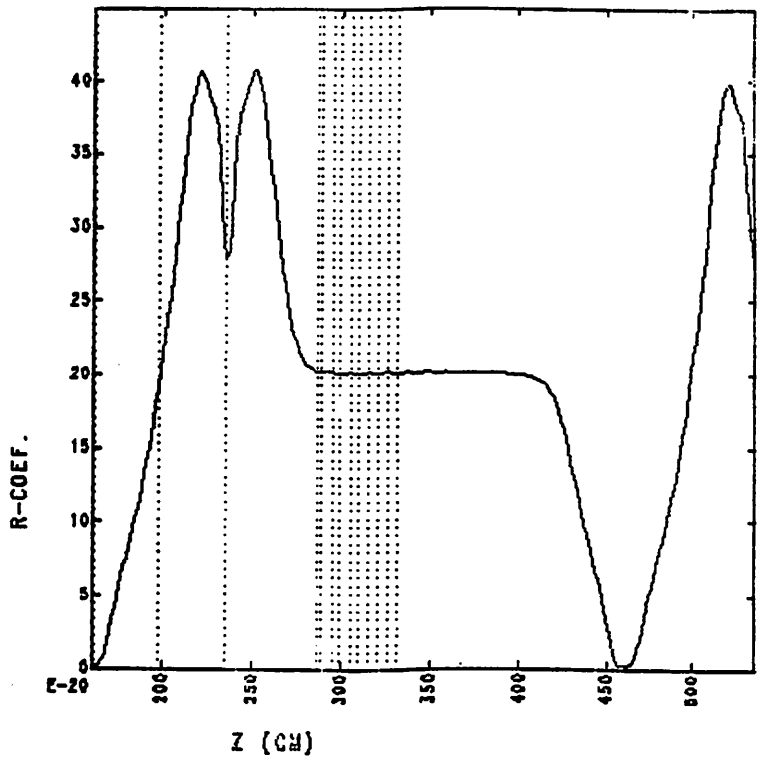
R-COEF.
E-20
Z (CM)

(f)

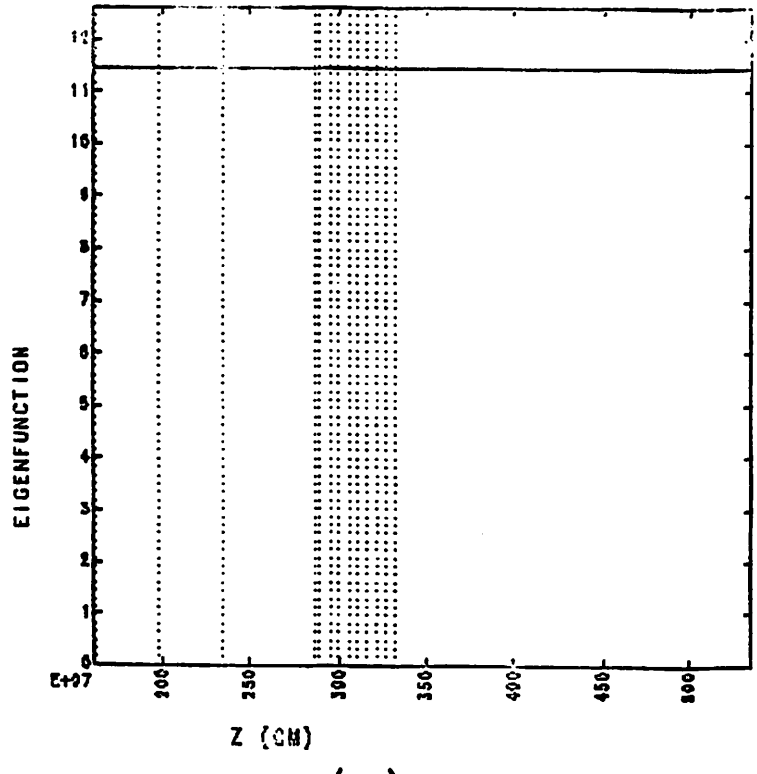
EIGENFUNCTION
E+07
Z (CM)

(g)

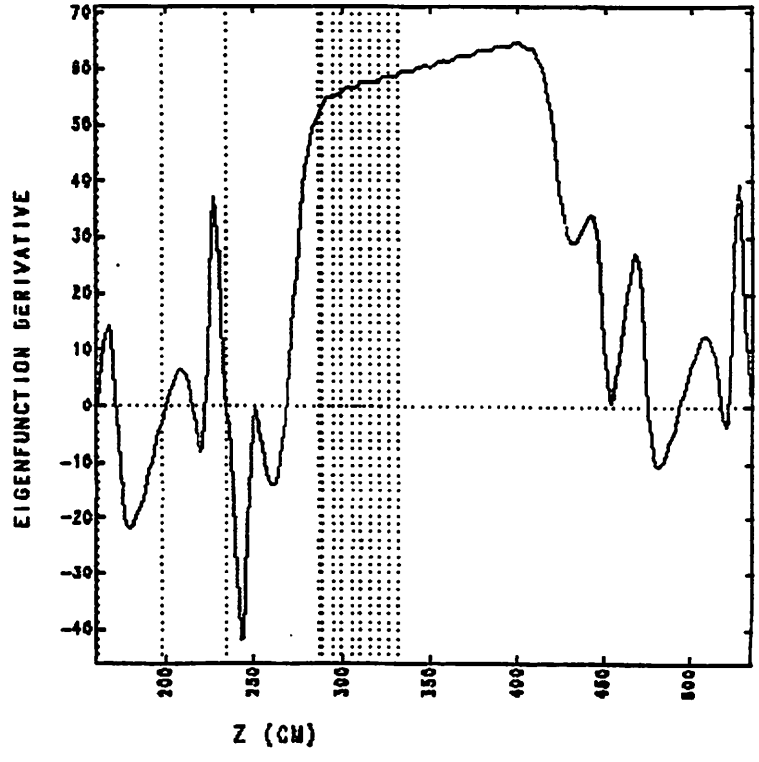
EIGENFUNCTION DERIVATIVE
Z (CM)

(h)

Fig. 5

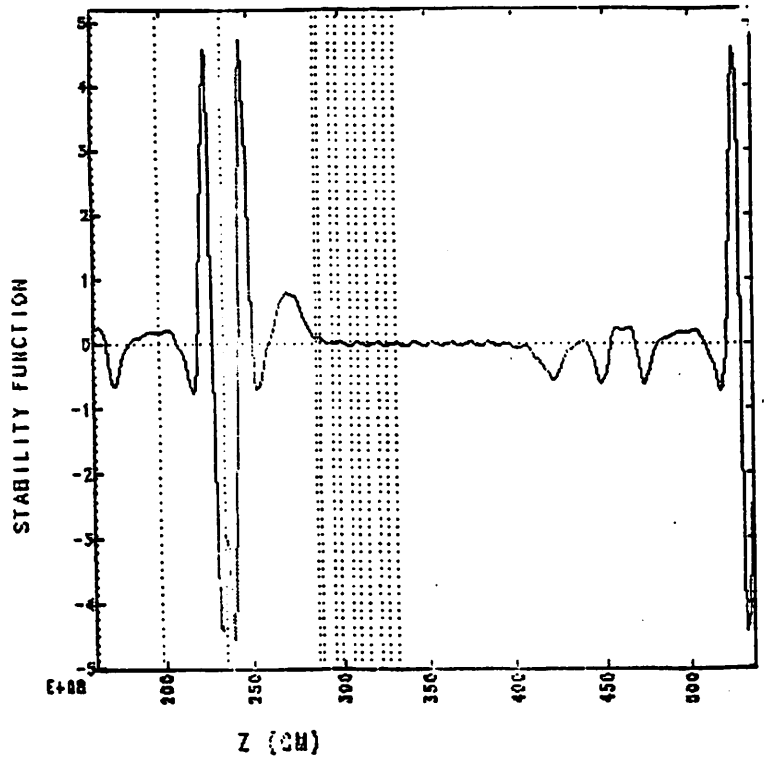
STABILITY FUNCTION
E+00
Z (CM)

(i)

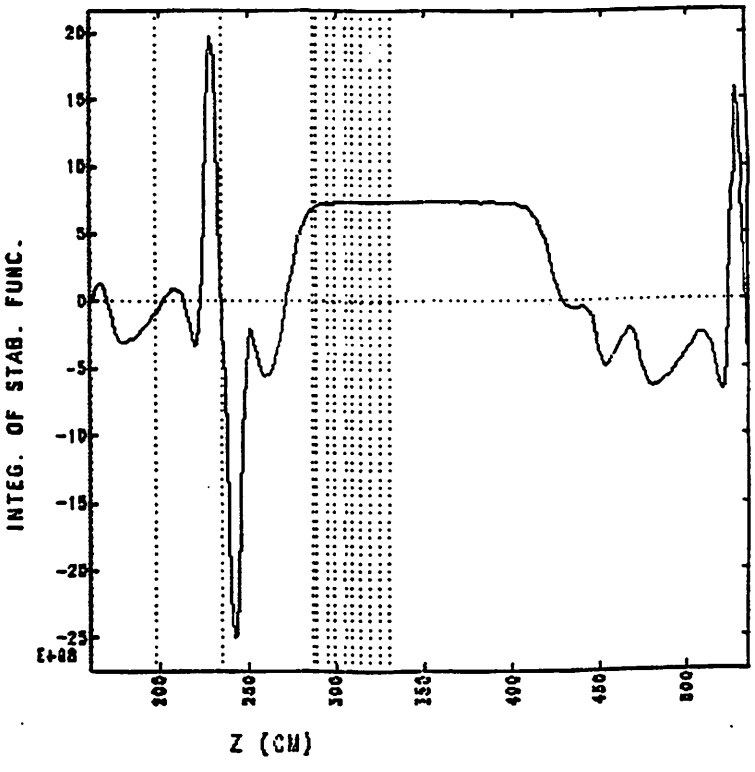
INTEG. OF STAB. FUNC.
E+00
Z (CM)

(j)

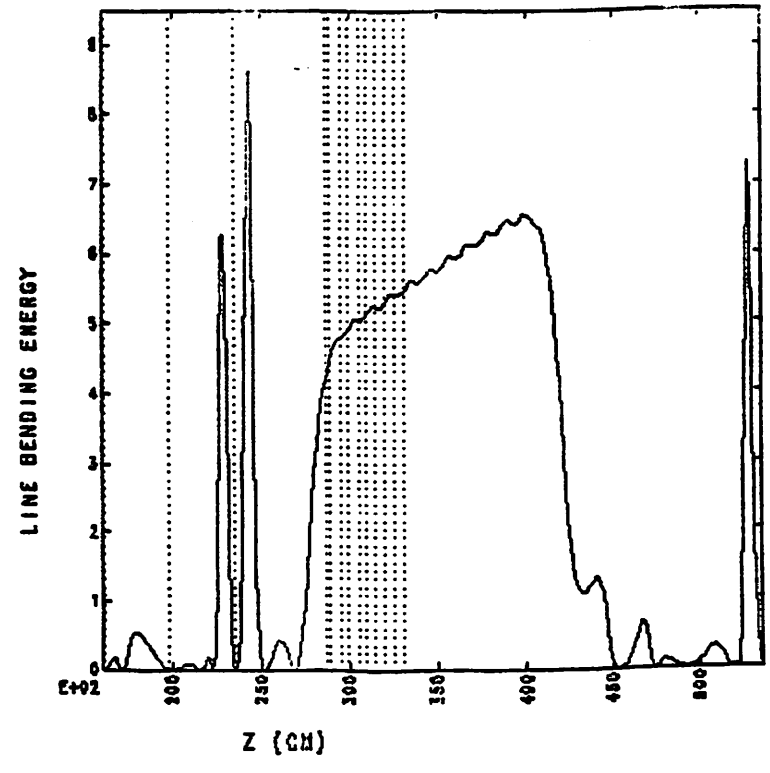
LINE BENDING ENERGY
E+02
Z (CM)

(k)

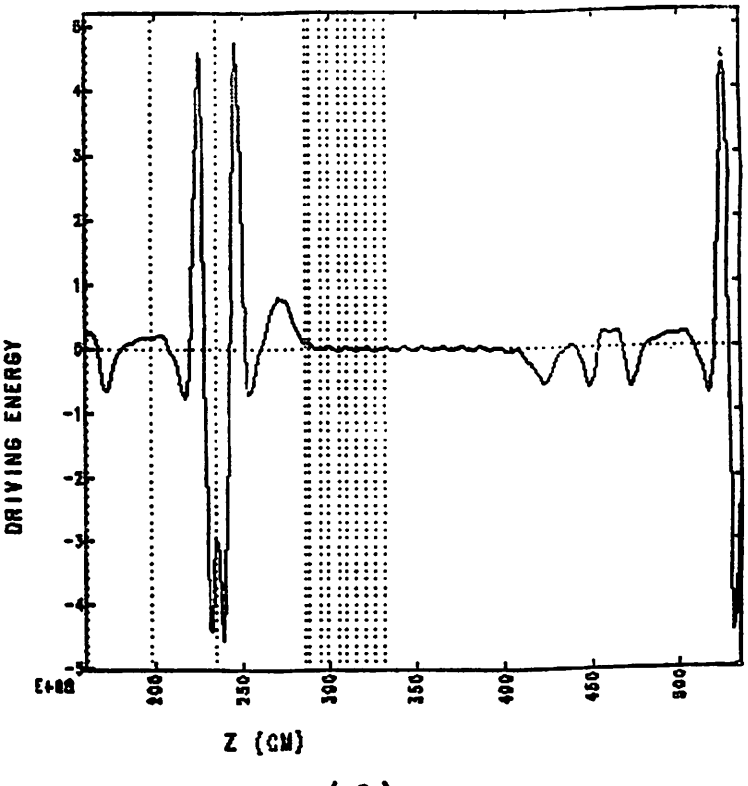
DRIVING ENERGY
E+00
Z (CM)

(ℓ)

Fig. 5

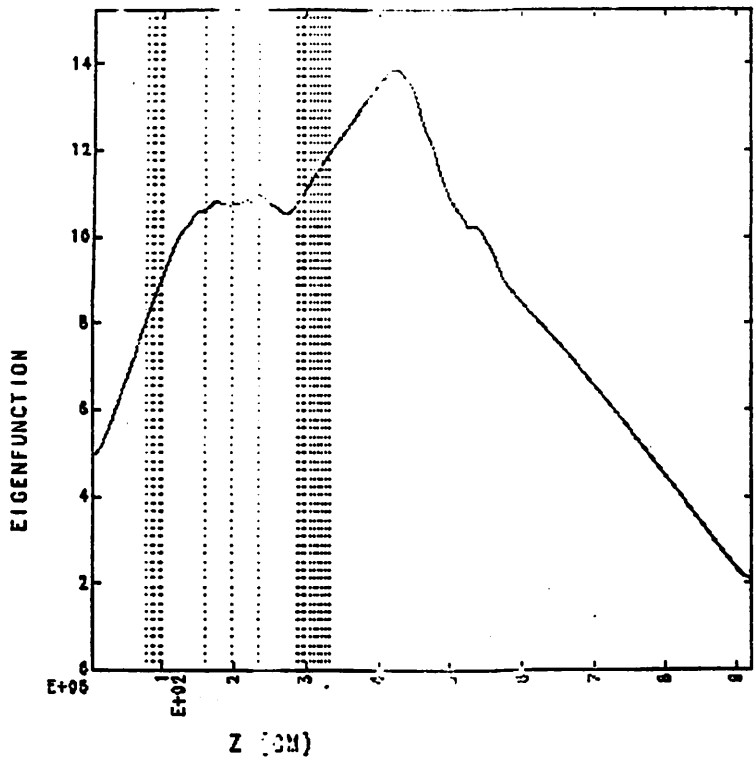
EIGENFUNCTION
Z (CM)

(a)

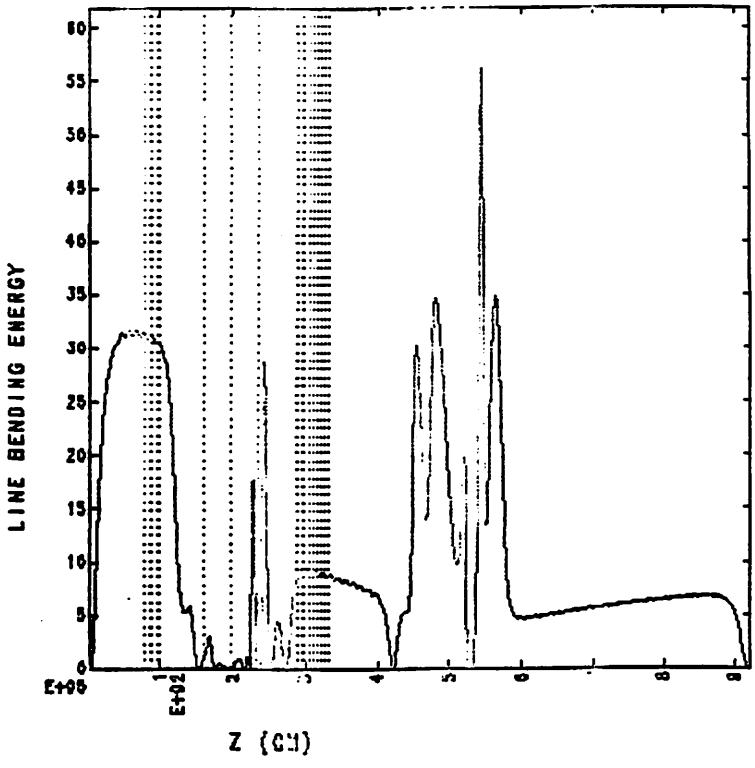
LINE BENDING ENERGY
Z (CM)

(b)

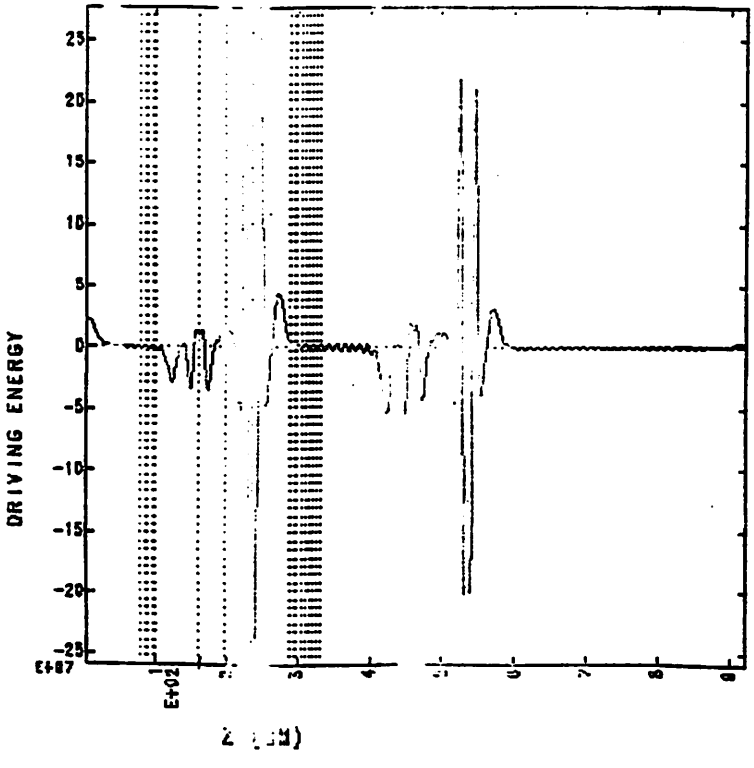
DRIVING ENERGY

(c)

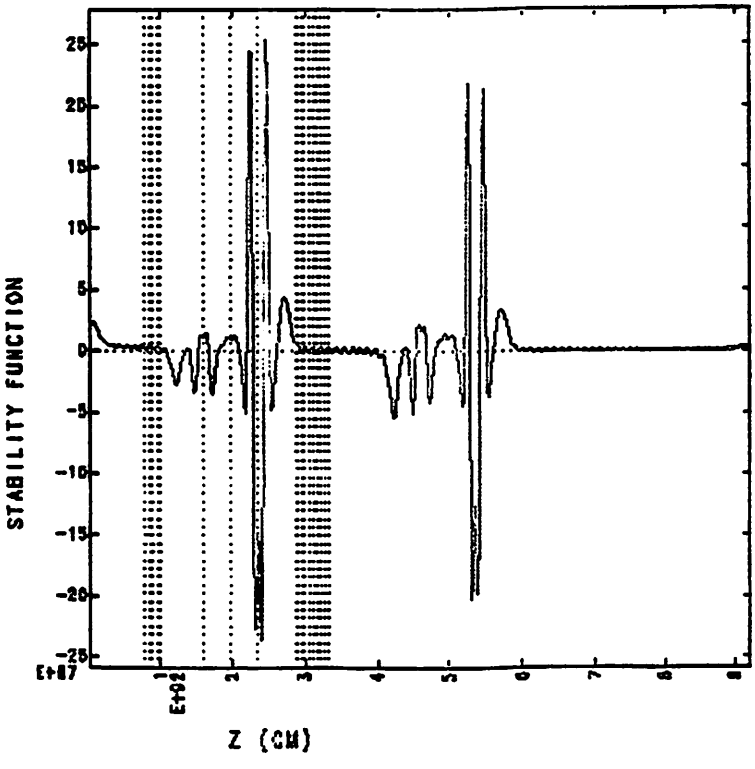
STABILITY FUNCTION
Z (CM)

(d)

Fig. 6

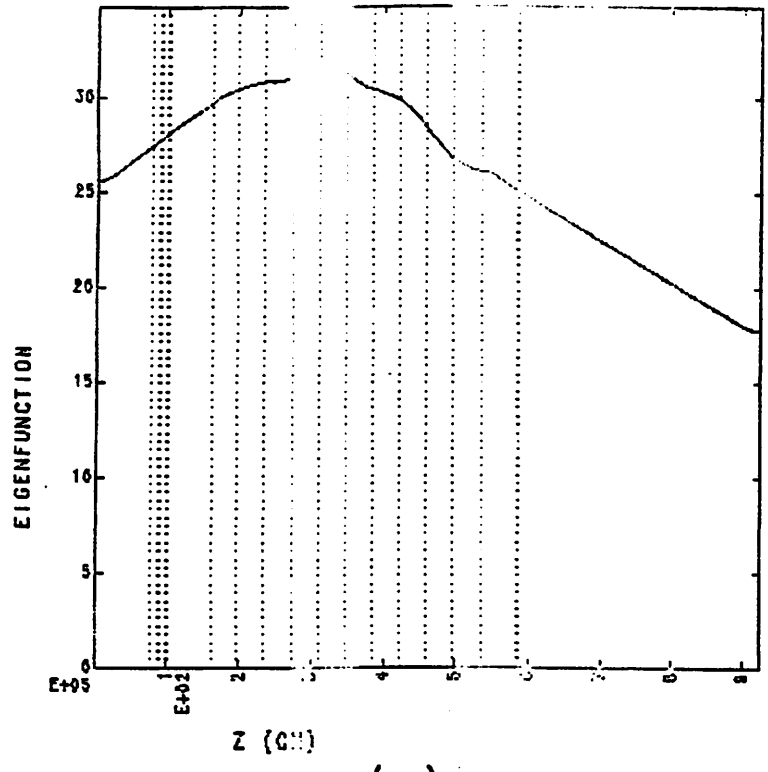
EIGENFUNCTION
Z (CM)

(a)

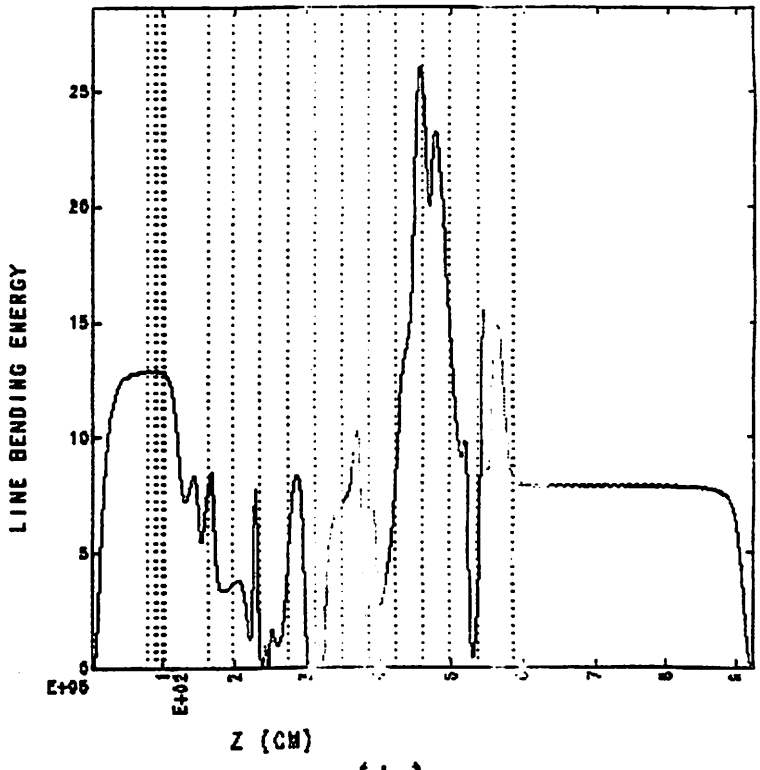
LINE BENDING ENERGY
Z (CM)

(b)

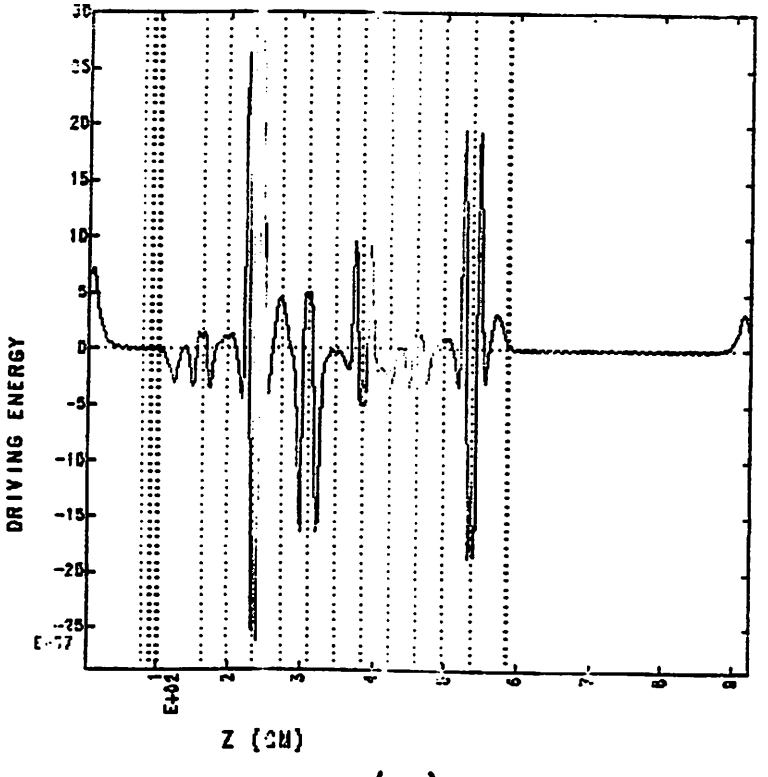
DRIVING ENERGY
Z (CM)

(c)

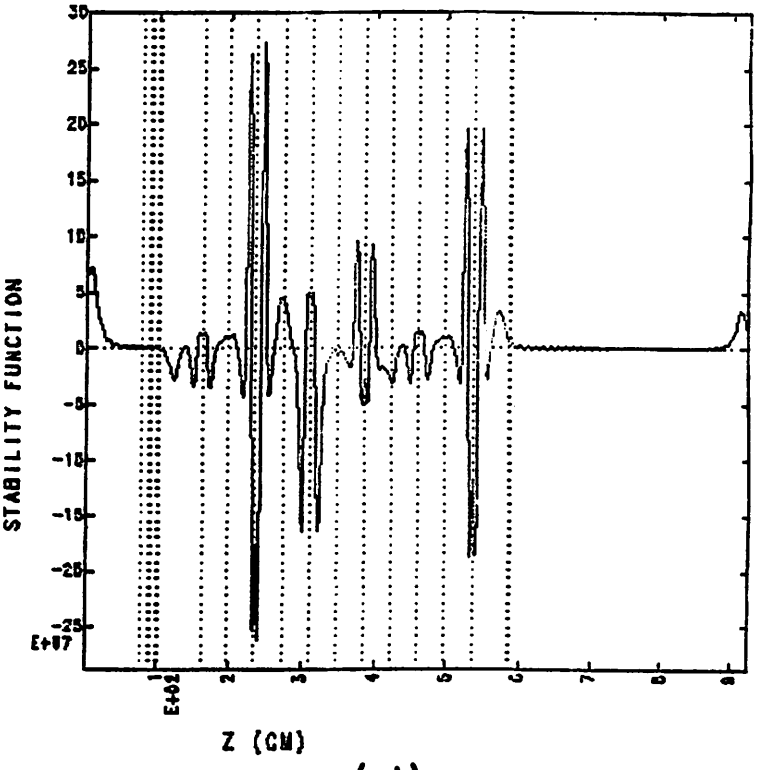
STABILITY FUNCTION
Z (CM)

(d)

Fig.7

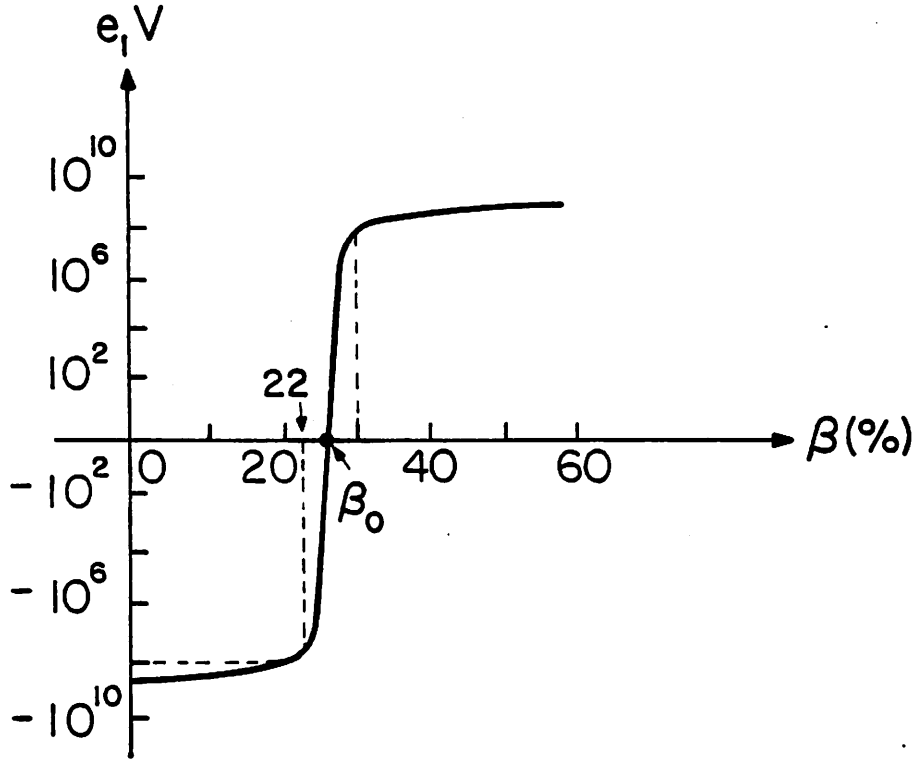

Fig. 8